

# A global wave parameter database for geophysical 1 applications. Part 3: improved forcing and spectral 2 resolution

Matias Alday<sup>1,1,1,1</sup>, Mickael Accensi<sup>1,1,1,1</sup>, Fabrice Ardhuin<sup>1,1,1,1</sup>, and Guillaume Dodet<sup>1,1,1</sup>

<sup>1</sup>LOPS

November 30, 2022

## Abstract

9 Numerical wave models are used for a wide range of applications, from the global ocean to coastal scales. Here we report on significant improvements compared to the previous hindcast by Rascle and Ardhuin (2013). This result was obtained by updating forcing fields, adjusting the spectral discretization and retuning wind wave growth and swell dissipation parameters. Most of the performance analysis is done using significant wave heights ( $H_s$ ) from the recent re-calibrated and denoised satellite altimeter data set provided by the European Space Agency Climate Change Initiative (ESA-CCI), with additional verification using spectral buoy data. We find that, for the year 2011, using wind fields from the recent ERA5 reanalysis provides lower scatter against satellite  $H_s$  data compared to historical ECMWF operational analyses, but still yields a low bias on wave heights that can be mitigated by re-scaling wind speeds larger than 20 m/s. Alternative blended wind products can provide more accurate forcing in some regions, but were not retained because of larger errors elsewhere. We use the shape of the probability density function of  $H_s$  around 2 m to fine tune the swell dissipation parameterization. The updated model hindcast appears to be generally more accurate than the previous version, and can be more accurate than the ERA5  $H_s$  estimates, in particular in strong current regions and for  $H_s > 7$  m.

1     A global wave parameter database for geophysical  
2     applications. Part 3: improved forcing and spectral  
3     resolution

4     Matias Alday<sup>a</sup>, Mickael Accensi<sup>a</sup>, Fabrice Ardhuin<sup>a,b</sup>, Guillaume Dodet<sup>a</sup>

5     <sup>a</sup>*Univ. Brest, CNRS, Ifremer, IRD, Laboratoire d'Océanographie Physique et Spatiale,*  
6     *Brest, France*

7     <sup>b</sup>*Scripps Institution of Oceanography, University of California San Diego, La Jolla,*  
8     *California*

---

9     **Abstract**

Numerical wave models are used for a wide range of applications, from the global ocean to coastal scales. Here we report on significant improvements compared to the previous hindcast detailed in Part 2 of the present study by Rascle and Ardhuin (2013). This result was obtained by updating forcing fields, adjusting the spectral discretization and retuning wind wave growth and swell dissipation parameters. Most of the model calibration and performance analysis is done using significant wave heights ( $H_s$ ) from the recent re-calibrated and denoised satellite altimeter data set provided by the European Space Agency Climate Change Initiative (ESA-CCI), with additional verification using spectral buoy data. We find that, for the year 2011, using wind fields from the recent ERA5 reanalysis provides lower scatter against satellite  $H_s$  data compared to historical ECMWF operational analyses, but still yields a low bias on wave heights that can be mitigated by re-scaling wind speeds larger than 20 m/s. Alternative blended wind products can provide more accurate forcing in some regions, but were not retained because of larger errors elsewhere. We use the shape of the probability density function of  $H_s$  around 2 m to fine tune the swell dissipation parameterization. The updated model hindcast appears to be generally more accurate than the previous version, and can be more accurate than the ERA5  $H_s$  estimates, in particular in strong current regions and for  $H_s > 7$  m.

10     *Keywords:* Wind-generated waves, WAVEWATCH III

---

## 1. Introduction

Spectral wave models are routinely used for many applications in Earth sciences and ocean engineering. Global and regional wave datasets generated through models such as WAM (WAMDI Group, 1988; Bidlot, 2005) or WAVEWATCH III® (The WAVEWATCH III® Development Group, 2019) have helped to improve our understanding of the wind-generated wave dynamics, estimate ocean-atmosphere interactions (e.g. surface drift and air-sea fluxes), analyze extreme events occurrences, define operational conditions for shipping, offshore and port activities, and assess wave energy resources, just to name a few examples. New applications, for example in seismology (e.g. Lecocq et al., 2019) or infrasound monitoring (De Carlo et al., 2021) are made possible by the ever increasing quality of modeled wave spectra and associated parameters.

The global hindcasts presented in Part 1 (Rascle et al., 2008) and Part 2 (Rascle and Ardhuin, 2013), and the Arctic hindcast of Stopa et al. (2016b) are unique in providing wave parameters in an "Earth System" context, including wave-related fluxes of momentum and energy between the ocean, atmosphere and sea ice. These hindcasts have been used in a wide range of applications, including as a source of boundary conditions for coastal models (Roland and Ardhuin, 2014; Boudière et al., 2013), air-sea fluxes and upper ocean mixing (Wunsch and Ferrari, 2009), surface drift of kelp or plastics (Fraser et al., 2018; Onink et al., 2019; Dobler et al., 2019), and the investigation of microseisms (e.g. Nishida and Takagi, 2016; Retailleau et al., 2017). For most open ocean regions, the accuracy of significant wave height ( $H_s$ ) estimates is typically better than 10%, with great benefits for the safety of life at sea, but for some regions, in enclosed seas, regions of strong currents, and near the sea ice,  $H_s$  errors typically exceed 20%, and other parameters can be much less accurate, in particular the shape of the frequency spectrum, the height of swells or the directional spreading (Stopa et al., 2016b). The reasons for these errors, and some first steps to reduce them, are the main topic of the present paper. In general the quality of numerical wave model output is a function of at least three factors, in decreasing order of importance. First, the accuracy of forcing fields (e.g. Cavaleri and Bertotti, 1997), second, the realism of parameterization of processes representing spectral wave evolution (e.g. Ardhuin et al., 2010) and third, the numerical choices made to integrate the Wave Action Equation, namely discretization and numerical schemes (e.g. Tolman, 1995; Roland and Ardhuin, 2014).

The present paper presents the effect of adjustment to model parameterizations in section 2, the impact of forcing field choices in section 3, and the influence of model discretization in section 4. We briefly discuss in section 5 alternative parameterizations that can lead to clear improvements for some parameters most sensitive to the higher frequencies of the wave spectrum but that, so far, have not led to improvements in  $H_s$  estimates and will probably require further adjustments and have thus not yet been used for the hindcast presented here. The global validation presented in section 6 shows a clear improvement on sea state parameters produced by [Rascle and Ardhuin \(2013\)](#) and, for specific conditions, also an improvement on the  $H_s$  estimates in the ERA5 reanalysis. Conclusions follow in section 6.

## 2. Model setup

### 2.1. Forcing fields

Because waves are forced by the wind, are damped by sea ice, and are strongly modified by currents, any improvement in the knowledge of these three forcing fields should result in better wave model results.

One of the main features in the generation of the wave hindcast analyzed in the present study, is the utilization of the wind fields from the fifth generation ECMWF atmospheric reanalyses of the global atmosphere, ERA5 ([Hersbach et al., 2020](#)), and the introduction of satellite-derived merged surface current product that combines geostrophic and Ekman currents, as produced by the Copernicus Marine Environment Monitoring System (CMEMS). The ERA5 reanalysis was developed using 4D-Var data assimilation from the Integrated Forecast System (IFS) model cycle 41r2. The number of observations assimilated from different measurement sources goes from 0.75 million per day in 1979 to approximately 24 million in 2018. The hourly output wind fields with a 31 km horizontal grid resolution, represents a clear increase in detail compared with some of its predecessors, like ERA-Interim ([Dee et al., 2011](#)). Still, the limited horizontal resolution makes the ERA5 wind fields less well resolved than those of recent ECMWF operational analyses that use a T799 Gaussian grid with an equivalent resolution of 25 km. [Rivas and Stoffelen \(2019\)](#) showed that ERA5 winds have a root mean square difference with the ASCAT winds that is 20% lower compared to ERA-Interim. Still, at wind speeds above 20 m/s, ERA5 biases may be as large as -5 m/s ([Pineau-Guillou et al., 2018](#)), which should have a very important impact on waves modeled with ERA5 winds.



The surface current fields were taken from the CMEMS-Globcurrent product (Global Ocean Multi Observation Product, MULTIOBS\_GLO\_PHY\_REP\_015\_004), with a resolution of 3 hour in time, and 0.25 degrees in latitude and longitude. This current field is the sum of geostrophic and Ekman components based on the method of [Rio et al. \(2014\)](#), using an updated mean dynamic topography (MDT) from CNES-CLS ([Mulet et al., 2021](#)), which is key for the reconstruction of the ocean absolute dynamic topography from altimetry data. With the geostrophic approximation, the MDT is used to estimate surface currents.

Finally, the ice concentration is taken from the Ifremer SSMI-derived daily product ([Girard-Ardhuin and Ezraty, 2012](#)). For ice thickness, that matters most near the ice edge where it is poorly known, we have used a constant 1 m ice thickness. Partial blocking of waves by icebergs is represented following [Ardhuin et al. \(2011\)](#) using the Ifremer-Altiberg icebergs distribution database [Tournadre et al. \(2015\)](#).

## 2.2. Adjusted parametrizations and parameters

Atmosphere-wave interactions include both wave generation as parametrized by [Janssen \(1991\)](#) with modifications by [Bidlot et al. \(2005, 2007\)](#) and swell damping caused the air-sea friction effect described by [Ardhuin et al. \(2009\)](#). The details and adjustments of these parametrizations are described in [Ardhuin et al. \(2010\)](#), and [Leckler \(2013\)](#). Here we only recall equations where the parameters that we have tuned in the present work are included. A more comprehensive description can be found in [The WAVEWATCH III® Development Group \(2019\)](#).

In particular, the wind input source term was reduced by using a modified friction velocity  $u_*$  with a frequency dependent term  $u'_*$ , similar to what was done by [Chen and Belcher \(2000\)](#). Eqs. (20) in [Ardhuin et al. \(2010\)](#) is

$$S_{\text{atm}}(f, \theta) = S_{\text{out}}(f, \theta) + \frac{\rho_a}{\rho_w} \frac{\beta_{\text{max}}}{\kappa^2 \exp(Z) Z^4 \left(\frac{u_*}{C}\right)^2} \quad (1)$$

$$\times \max\{\cos(\theta - \theta_u), 0\}^p \sigma F(f, \theta) \quad (2)$$

where:  $S_{\text{out}}$  is the energy flux from the ocean to the atmosphere (swell dissipation term),  $Z = \log(\mu)$ , with  $\mu$  the dimensionless critical height as given by [Janssen \(1991, eq. 16\)](#).  $\rho_a$  is the air density,  $\rho_w$  the water density and  $\kappa$  is von Kármán's constant.  $C$  is the wave phase speed,  $\theta$  the wave direction,  $\theta_u$

115 the wind direction, and  $\sigma$  the wave relative frequency ( $2\pi/f_r$ , observed from  
116 a reference frame moving with the mean current).

117 In eq. (1)  $\beta_{\max}$  is a non-dimensional wind-wave growth coefficient that  
118 has been used as a tuning parameter to calibrate for wind strength biases  
119 (e.g. [Stopa et al., 2019](#)). We will revisit this tuning for ERA5 winds in the  
120 present paper.

121 The swell dissipation parameterization is based on observations of ocean  
122 swell evolution from satellite data ([Ardhuin et al., 2009](#)). It includes expres-  
123 sions to take into account the effects of the transitions from (linear) viscous  
124 boundary layer to (non-linear) turbulent boundary layer. The smoothing  
125 between these two regimes accounts for the Rayleigh distribution of wave  
126 heights ([Perignon et al., 2014](#)). The negative part of the wave-atmosphere  
127 interaction, is thus parameterized as follows,

$$S_{\text{out}}(k, \theta) = r_{\text{vis}} S_{\text{out,vis}}(k, \theta) + r_{\text{tur}} S_{\text{out,tur}}(k, \theta), \quad (3)$$

128 where the two weights give the relative importance of viscous and turbu-  
129 lent attenuation, and are controlled by the ratio of the significant Reynolds  
130 number  $\text{Re} = 2u_{\text{orb,s}}H_s/\nu_a$  and its critical value  $\text{Re}_c$ .

$$r_{\text{vis}} = 0.5 [1 - \tanh((\text{Re} - \text{Re}_c)/s_7)] \quad (4)$$

$$r_{\text{tur}} = 0.5 [1 + \tanh((\text{Re} - \text{Re}_c)/s_7)]. \quad (5)$$

131 Based on the analogy with oscillatory bottom boundary layers,  $\text{Re}_c$  was ini-  
132 tially set to  $1.5 \times 10^5$ .

133 Wave energy loss to the ocean is dominated by wave breaking, and param-  
134 eterized following the saturation-based breaking ideas of [Phillips \(1985\)](#). An  
135 ad hoc "cumulative term" was added to enhance the dissipation of relatively  
136 short waves ([Banner and Morison, 2006](#); [Ardhuin et al., 2010](#)). Alternatives  
137 are discussed in section 5.

138 Finally, to reduce computational costs, we have used the Discrete Interac-  
139 tion Approximation (DIA [Hasselmann and Hasselmann, 1985](#)), to represent  
140 the 4-wave nonlinear interactions. This rather crude parameterization in-  
141 duces errors that are partly corrected by the other adjusted source terms in  
142 the Wave Action Equation ([Banner and Young, 1994](#)).

### 143 2.3. Spectral and spatial discretization

144 The wave spectrum is discretized in 24 directions, equivalent to a 15°  
 145 directional resolution, and 36 exponentially spaced frequencies from 0.034 to  
 146 0.95 Hz, with a 1.1 increment factor from one frequency to the next. The  
 147 selected frequency range represents a departure from our previous hindcasts  
 148 (Rascle and Ardhuin, 2013), in which a narrower frequency range was em-  
 149 ployed, from 0.037 to 0.71 Hz. Although the parameterizations used here  
 150 are not very accurate for frequencies above 3 times the wind sea peak (e.g.  
 151 Peureux et al., 2018), the extension to higher frequencies allows to better  
 152 capture the variability of the wave spectrum for very low wind speeds or  
 153 very short fetches. The lower frequencies are there to let the spectrum de-  
 154 velop for the most severe storm cases (Hanafin et al., 2012). We have used  
 155 the third order Upwind Quickest advection schemes (Leonard, 1991) for both  
 156 spatial and spectral advection, and the correction for the Garden Sprinkler  
 157 Effect proposed by Tolman (2002).

158 All the model testing and tuning presented in section 2 was performed  
 159 over a near-global grid with a spatial resolution of 0.5°, from 78° S to 83° N  
 160 in latitude. However, all the other results, including the final hindcast, use  
 161 a multi-grid system (Tolman, 2008; Chawla et al., 2013) in which regional  
 162 grids provide a refinement near the coasts, the ice edge, and in regions of  
 163 strong currents. A total of 7 nested grids were placed within the global  
 164 grid, 6 regular grids and 1 curvilinear grid for the Arctic region. Details of  
 165 the nested grids are provided in table 1 and Fig. 1. As shown in Fig. 1,  
 166 the boundaries of the high resolution domains (in color) generally follow the  
 167 coast at 500 km distance, including regions around Hawaii and the Tuamotus  
 168 for the East Pacific grid, and the Azores for the North-East Atlantic grid.  
 169 The regions in white are only covered with the global 0.5 degree resolution.  
 170 The boundary conditions from a lower rank grid are taken at the edges of  
 171 the colored regions in Fig. 1, and the higher rank grid results are spatially  
 172 averaged to give the lower rank grid solution where these overlap (Tolman,  
 173 2008).

174 The benefits of the multi-grid system are particularly discussed in section  
 175 4.1. Compared to Rascle and Ardhuin (2013), including the Arctic grid  
 176 allowed to provide a truly global wave hindcast.

### 177 2.4. Model tuning

178 The value of  $\beta_{\max}$  in eq. (1),  $s_7$  and  $\text{Re}_c$  in eqs. (4) and (5) have been  
 179 adjusted to minimize the model differences against satellite altimeter mea-

Sub-Grid Name	Region	Grid type	Spatial resolution	Rank
ATNE-10M	North-East Atlantic	regular	1/6°	2
ATNW-10M	North-West Pacific	regular	1/6°	3
AFRICA-10M	Africa	regular	1/6°	3
PACE-10M	East Pacific	regular	1/6°	2
CRB-3M	Carribean Sea	regular	1/20°	3
NC-3M	New Caledonia and Vanuatu	regular	1/20°	3
ARC-12K	Arctic Ocean	curvilinear	12 km	4

Table 1: Nested grids characteristics. Global grid is defined as rank 1.

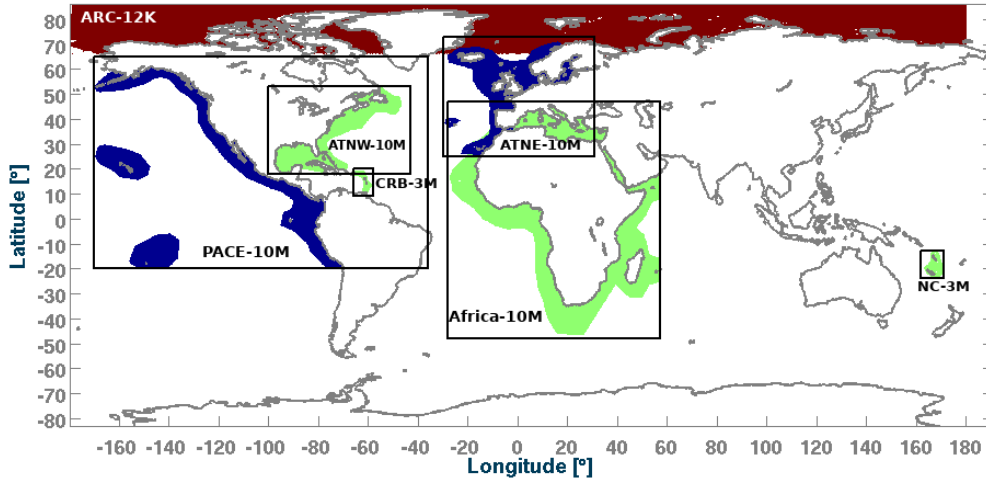


Figure 1: Sub-Grids nesting layout for multi-grid tests. Colors indicate areas where computations are performed and grids' rank in the nesting scheme: Blue is rank 2, Green is rank 3, and Red is rank 4.

180 surements of  $H_s$  by the Jason-2 mission for the year 2011, using the European  
 181 Space Agency Climate Change Initiative data set (Dodet et al., 2020). We  
 182 use a full year for calibration to properly sample all types of sea states in  
 183 all seasons, and the year 2011 has been chosen because it had the highest  
 184 wave heights ever recorded Hanafin et al. (2012), and this allows a sampling  
 185 of the most extreme conditions. The variable used is the "denoised" signifi-  
 186 cant wave height, at 1 Hz (approximately 7 km) resolution. The model tests  
 187 performed and associated parameter values are listed in table 2. All test sim-  
 188 ulations are 1-year hindcasts with data output frequency of 3 hours. These  
 189 tests also include some wind bias correction. This correction is defined as a

190 piece-wise linear correction, with modeled wind speeds above  $U_c$  multiplied  
191 by a factor  $x_c$  as follows,

$$U_{10,\text{corr}} = U_{10,\text{raw}} + x_c \max \{U_{10,\text{raw}} - U_c, 0\}. \quad (6)$$

Name for set of parameters	$\beta_{\text{max}}$	$s_7$	$\text{Re}_c$	$U_c$ (m/s)	$x_c$
T471f	1.33	$3.60 \times 10^5$	$1.50 \times 10^5$	–	–
<b>T471</b>	1.43	$3.60 \times 10^5$	$1.50 \times 10^5$	–	–
Bm1.5	1.50	$3.60 \times 10^5$	$1.50 \times 10^5$	–	–
Bm1.65	1.65	$3.60 \times 10^5$	$1.50 \times 10^5$	–	–
Bm1.7	1.70	$3.60 \times 10^5$	$1.50 \times 10^5$	–	–
Bm1.75	<b>1.75</b>	$3.60 \times 10^5$	$1.50 \times 10^5$	–	–
Bm1.65-W01	1.65	$3.60 \times 10^5$	$1.50 \times 10^5$	20	1.05
Bm1.65-W02	1.65	$3.60 \times 10^5$	$1.50 \times 10^5$	21	1.05
Bm1.65-W03	1.65	$3.60 \times 10^5$	$1.50 \times 10^5$	23	1.08
Bm1.65-W04	1.65	$3.60 \times 10^5$	$1.50 \times 10^5$	22	1.05
Bm1.7-W02	1.70	$3.60 \times 10^5$	$1.50 \times 10^5$	21	1.05
Bm1.7-W03	1.70	$3.60 \times 10^5$	$1.50 \times 10^5$	23	1.08
Bm1.7-W04	1.70	$3.60 \times 10^5$	$1.50 \times 10^5$	22	1.05
Bm1.75-W02	<b>1.75</b>	$3.60 \times 10^5$	$1.50 \times 10^5$	21	1.05
Bm1.75-W03	<b>1.75</b>	$3.60 \times 10^5$	$1.50 \times 10^5$	23	1.08
Bm1.75-W04	<b>1.75</b>	$3.60 \times 10^5$	$1.50 \times 10^5$	22	1.05
Bm1.75-W02-s7-01	<b>1.75</b>	$3.96 \times 10^5$	$1.50 \times 10^5$	21	1.05
Bm1.75-W02-s7-02	<b>1.75</b>	$4.14 \times 10^5$	$1.50 \times 10^5$	21	1.05
Bm1.75-W02-s7-03	<b>1.75</b>	<b><math>4.32 \times 10^5</math></b>	$1.50 \times 10^5$	21	1.05
Bm1.75-W02-s7-03-s4-01	<b>1.75</b>	<b><math>4.32 \times 10^5</math></b>	$1.35 \times 10^5$	21	1.05
Bm1.75-W02-s7-03-s4-02	<b>1.75</b>	<b><math>4.32 \times 10^5</math></b>	$1.20 \times 10^5$	21	1.05
<b>T475</b>	<b>1.75</b>	<b><math>4.32 \times 10^5</math></b>	<b><math>1.15 \times 10^5</math></b>	21	1.05

Table 2: Models parameters and their adjustments, in bold, leading to run T475. All parameters not specified here correspond to the default T471 parameterization (Raschle and Ardhuin, 2013; The WAVEWATCH III<sup>®</sup> Development Group, 2019). Variables  $\beta_{\text{max}}$ ,  $s_7$ ,  $\text{Re}_c$ ,  $U_c$  and  $x_c$  correspond to namelist parameters BETAMAX, SWELLF7, SWELLF4, WCOR1 and WCOR2 in the WW3 input files (see Appendix A for the full set of parameters).

192 The normalized root mean square difference (NRMSD), scatter index (SI)  
193 and normalized mean difference (NMD) were employed to assess the model  
194 - satellite discrepancy and its change when model parameterizations, forcing  
195 or discretization are modified. These statistical parameters were calculated  
196 for the entire domain and over a set of specific ocean regions (defined in table

197 3), for each 1-year test in table 2. They are defined as follows,

$$\text{NRMSD}(X) = \sqrt{\frac{\sum (X_{\text{mod}} - X_{\text{obs}})^2}{\sum X_{\text{obs}}^2}} \quad (7)$$

$$\text{SI}(X) = \sqrt{\frac{\sum [(X_{\text{mod}} - \overline{X_{\text{mod}}}) - (X_{\text{obs}} - \overline{X_{\text{obs}}})]^2}{\sum X_{\text{obs}}^2}} \quad (8)$$

$$\text{NMD}(X) = \frac{\sum (X_{\text{mod}} - X_{\text{obs}})}{\sum X_{\text{obs}}} \quad (9)$$

198 where  $X_{\text{obs}}$  and  $X_{\text{mod}}$  are the altimeter significant wave heights (denoised) and  
 199 the modelled  $H_s$  respectively. In particular for the tuning process,  $X_{\text{obs}}$  is the  
 200 along-track data from the altimeter, and  $X_{\text{mod}}$  is obtained by interpolating  
 201 the model output in space and time from the closest 4 grid points, into the  
 202 position of the altimeter measurement.

203 We note that other normalizations could be used (Mentaschi et al., 2015),  
 204 and in particular a larger scatter index is not always the indication of a  
 205 poorer model performance, in particular in the presence of large biases or  
 206 large fluctuations.

207 We particularly looked at differences for different ranges of observed val-  
 208 ues of  $H_s$ , binning all the model output as a function of the satellite values.  
 209 In general, for the model’s performance assessment, attention was only paid  
 210 to  $H_s$  larger than 1.0 m because  $H_s$  smaller than 0.75 m is not very accurate  
 211 due to limited sampling of the signal associated with the radar bandwidth  
 212 (Smith and Scharroo, 2015; Ardhuin et al., 2019).

213 Previous parameter settings defined as “T471” were used as a starting  
 214 point. After gradual increases of  $\beta_{\text{max}}$  without changing the other parameters  
 215 (sets T471f to Bm1.75 as defined in table 2), a persistent negative NMD for  
 216  $H_s$  values larger than 7 m is found, as illustrated in Fig. 2.

217 This behavior is expected to be related to an underestimation of wind  
 218 speeds in excess of 25 m/s in ECMWF IFS model results, including the  
 219 ERA5 data set, as analyzed by Pineau-Guillou et al. (2018). This wind-  
 220 speed dependent bias, which is not found with CFSR winds, was the main  
 221 motivation for introducing the wind speed correction in eq. (6).

222 After setting  $\beta_{\text{max}} = 1.75$ , wind speed corrections with the parameters  
 223 Bm1.75-W02 helped to reduce the wave heights underestimation in the 8–  
 224 14 m range (Fig. 3).

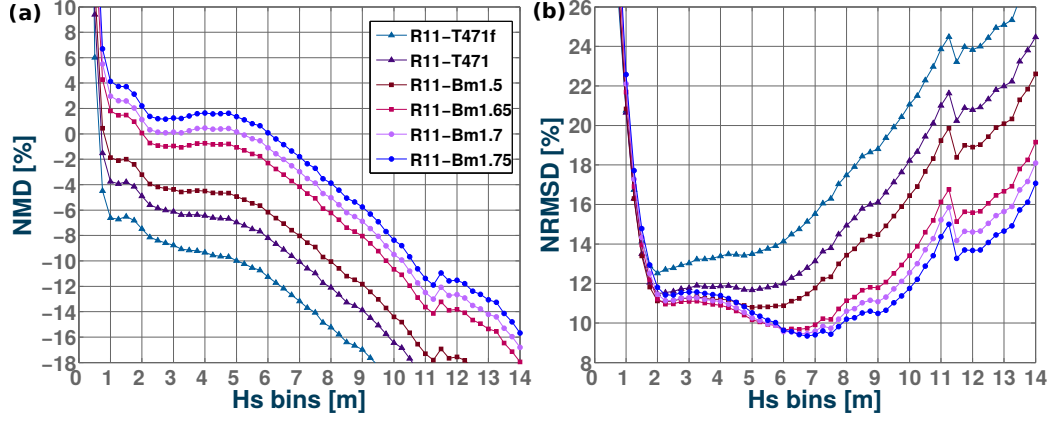


Figure 2: Error statistics for  $H_s$  for the  $\beta_{\max}$  sensitivity runs (a) Normalized mean difference between model runs – with parameters given in Table 2 – and the Jason-2 altimeter data, (b) normalized root mean square difference.

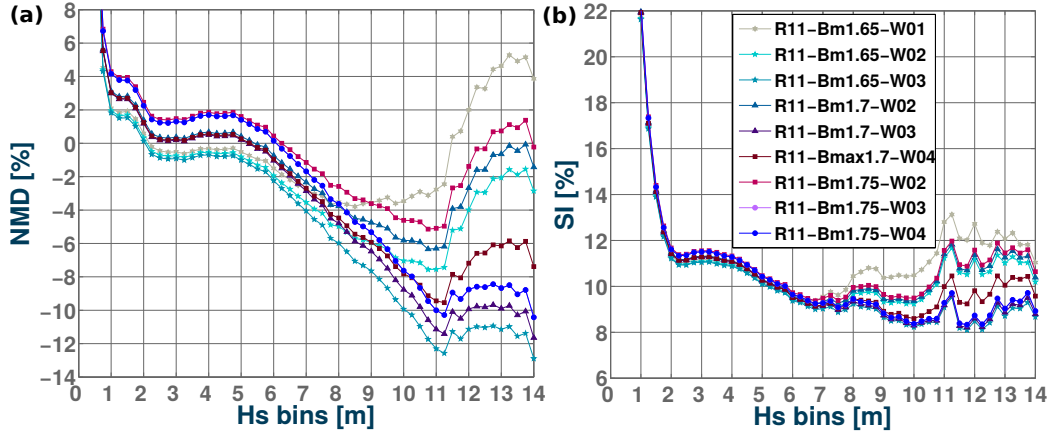


Figure 3: Error statistics for  $H_s$  for the wind correction sensitivity runs (a) Normalized mean difference between model runs – with parameters given in Table 2 – and the Jason-2 altimeter data, and (b) scatter index.

225 The wind speed  $U_c$  at which the correction kicks in is consistent with the  
 226 analysis of models and in situ wind data by Pineau-Guillou et al. (2018),  
 227 where it was demonstrated that typically strong winds above  $20 \text{ m s}^{-1}$  are  
 228 underestimated by the ECMWF models.

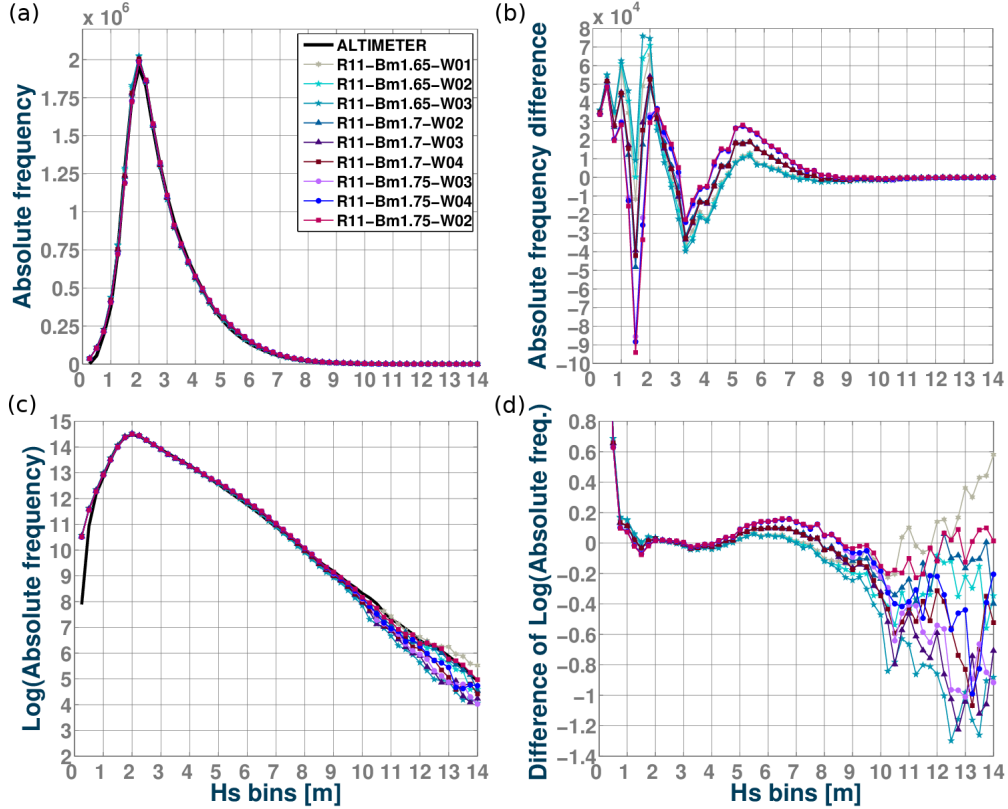


Figure 4: (a) Histogram of  $H_s$  values in the Jason-2 and co-located model simulations. (b) Differences between the model and altimeter histograms. Plots shown are from wind correction tests only. (c) Same as (a) but with a logarithmic scale. (d) Difference of logarithm of the modeled and measured  $H_s$  histograms.

229 Once the NMD and NRMSD were reduced, particular attention was paid  
 230 to the distribution of  $H_s$ . The applied changes in  $\beta_{\max}$  and wind correction  
 231 lead to more intense waves in storms and swells radiated from these storms.  
 232 As a result the swell dissipation necessarily needs further tuning, which is  
 233 done here by adjusting  $s_7$  and  $\text{Re}_c$ . This adjustment can be done using  
 234 wave spectra measurements from buoys, but also using the distribution of  
 235  $H_s$ . Indeed, the smoothing of swell dissipation was introduced in eq. (3) by



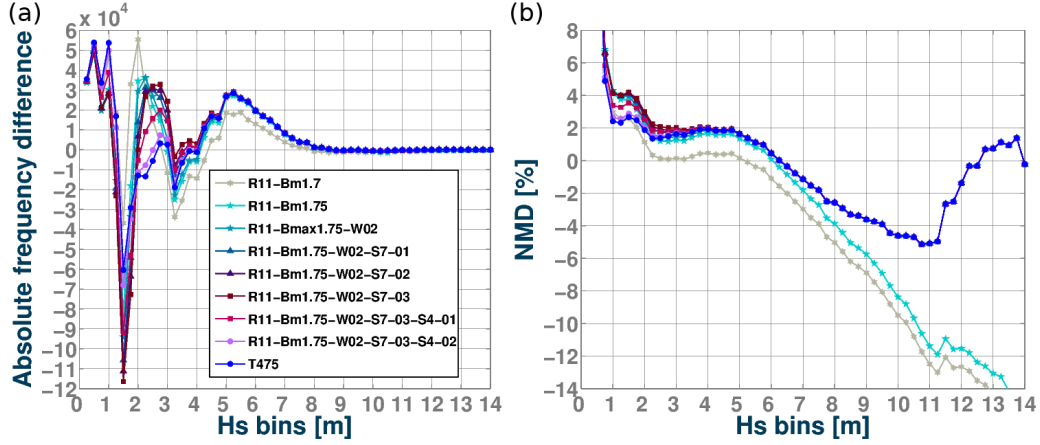


Figure 5: (a) Histogram of  $H_s$  values in the Jason-2 and model simulations absolute frequency of occurrence difference (WW3 - altimetry data). (b) Normalized mean bias. Plots shown are from  $s_7$  and  $Re_c$  sensitivity tests.

236 Leckler et al. (2013) to correct the sharp jump around 2 m in the distribution  
 237 of modeled  $H_s$  that was first noted by D. Vandemark (personal communi-  
 238 cation, 2012). It was only later rationalized as an effect of the Rayleigh  
 239 distribution of wave heights with turbulent boundary layers over the largest  
 240 waves in a group and viscous boundary layers over the lowest waves in a  
 241 group (Perignon et al., 2014; Stopa et al., 2016b). Fig. 4 shows the dis-  
 242 tribution of  $H_s$  in the model and observations. With panel b showing the  
 243 difference between model and observation to make the differences more visi-  
 244 ble for wave heights smaller than 8 m, and in panel d the difference of the log  
 245 of frequency of occurrence to see the deviations for larger  $H_s$ . Augmenting  
 246  $s_7$  from  $3.6 \times 10^5$  with the parameters s7-01 to  $4.32 \times 10^5$  with s7-03 spreads  
 247 the transition from viscous to turbulent dissipation over a wider range of  
 248  $H_s$  and tends to smooth the histogram of  $H_s$ . This corrects the bias in the  
 249 distribution around  $H_s = 2.0$  m but makes things worse around 1.5 m. To  
 250 correct those errors requires also shifting the transition Reynolds number  $Re_c$   
 251 to lower values in runs s4-01, s4-02 and s4-03 as shown in Fig. 5.a. These  
 252 later adjustments made it possible to match the occurrence of the highest  
 253 values of  $H_s$ , up to 14 m, as shown in Fig. 5.b.

254 Although  $H_s$  gives a very limited description of the sea state, the great  
 255 benefit of  $H_s$  altimeter data is their global coverage, and the differences  
 256 between model and observation over different regions of the world ocean can

also be revealing due to the different types of sea states found in these regions (Chen et al., 2002), but also due to different forcing by winds, currents and sea ice. Table 3 defines the different ocean regions for which we have looked at regional  $H_s$  statistics. Further analyses on effects over the directional spreading and other wave parameters based on in-situ measurements, are presented in section 5 and 6.3 respectively.

Region (basin)	Minimum Longitude [°]	Maximum Longitude [°]	Minimum Latitude [°]	Maximum Latitude [°]
North Atlantic	-80	-5	10	50
South Atlantic	-68	20	-54	-2
North Pacific	125	-100	5	60
South Pacific	150	-73	-54	-2
Indian Ocean	50	100	-30	25
Southern Ocean	-179.98	180	-70	-55
NO SOUTH	-179.98	180	-55	66

Table 3: Regions definition for performance analysis.

The adjustments of  $\beta_{\max}$  and wind intensities corrections showed particularly good improvements in the North and South Pacific. By only augmenting the  $\beta_{\max}$  value (for example in tests R11-Bm1.7 and R11-Bm1.75), an important decrease of the  $H_s$  occurrences is obtained around 2 m, especially in the South Pacific, but this comes at the price of an excess of  $H_s$  values in the 1–1.5 m range (Fig. 6).

Higher values of  $\beta_{\max}$  also reduced the overall negative bias in wave heights within the range of 1.5–7 m, with a further reduction of the negative NMD when the selected wind correction is applied. This specially improves the NMD for  $H_s$  of 7 to 11 m in the North Atlantic and South Pacific (Fig. 7). The South Pacific stands out as a region of high positive bias (Fig. 8).

Although it is possible that winds in the Southern Ocean may have specific biases due to a limited set of data used for assimilation, the state of the atmosphere is very much controlled by remote sensing data, including radiometers and scatterometers that are assimilated globally (Hersbach et al., 2020).

Another peculiarity of the Southern Ocean is the importance of the circumpolar current that generally flows from West to East. Not taking it into account is known to produce a large positive bias of the order of 20 cm

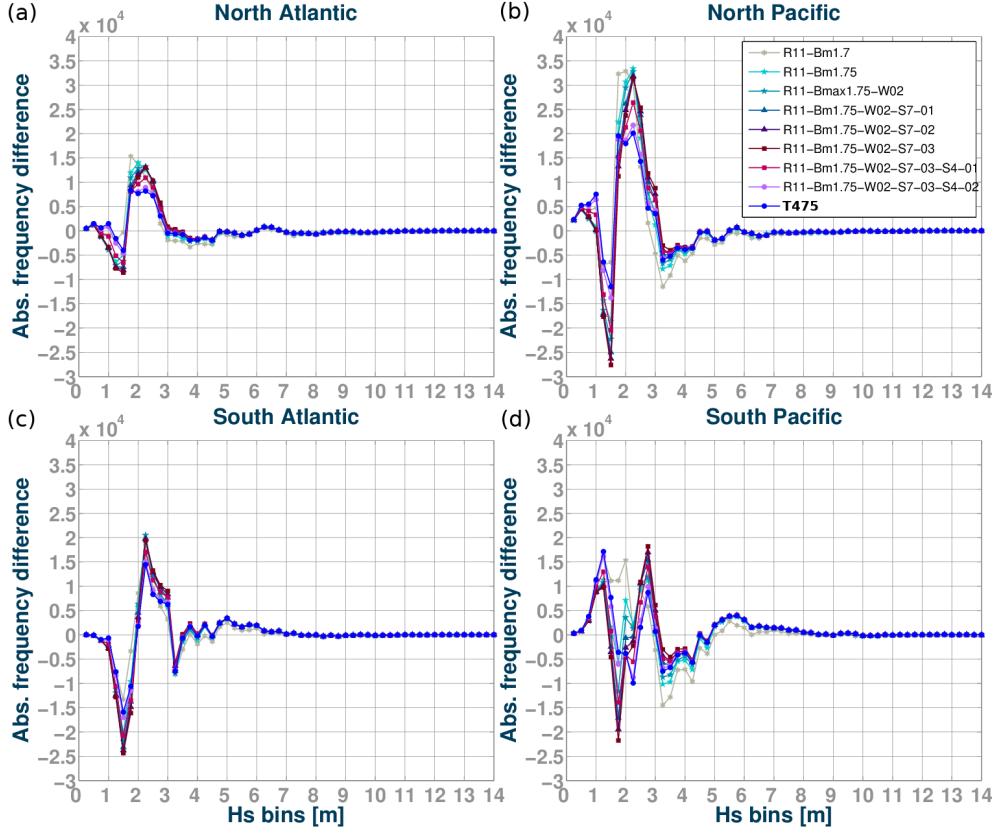


Figure 6:  $H_s$  absolute frequency of occurrence difference (WW3 - altimetry data) from Atlantic and Pacific basins.

in wave heights due to the relative wind effect (Rascle et al., 2008; Rapizo et al., 2018), and large gradients in  $H_s$  associated to refraction (Quilfen and Chapron, 2019). Indeed, the relevant wind speed for wave generation is the wind velocity minus the surface current velocity. However, these previous estimates use numerical models that are not very reliable for surface current estimates (ESA, 2019). Another effect specific to the Southern Ocean is the presence of both sea ice and icebergs, with a very large impact on wave heights (Ardhuin et al., 2011). The year 2011 has a rather large anomaly in iceberg numbers, although not as large as in 2009 (Tournadre et al., 2016). Finally, the details in sea ice concentration near the ice edge and the parameterizations of wave-ice interactions are another important source of uncertainties at latitudes south of  $55^\circ\text{S}$  (Doble and Bidlot, 2013; Ardhuin et al., 2020).

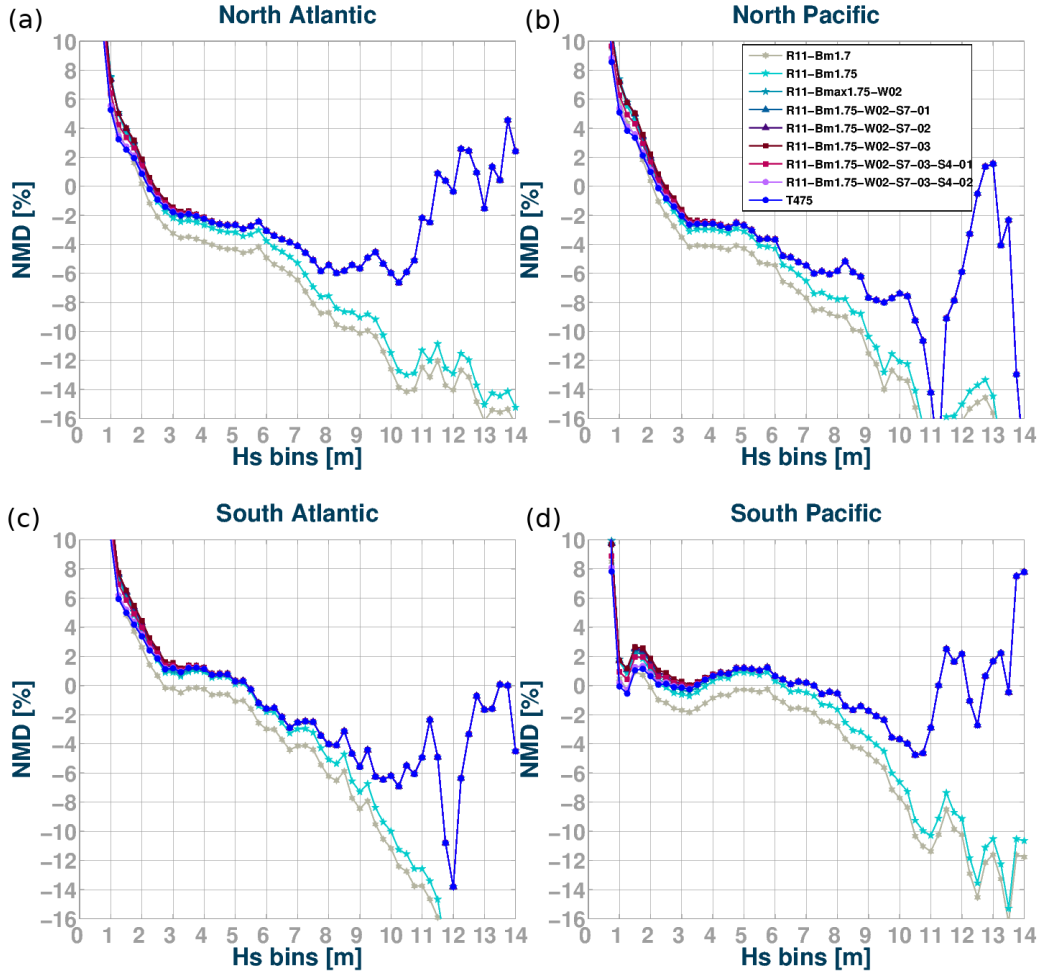


Figure 7:  $H_s$  NMD within Atlantic and Pacific basins as a function of observed wave heights.  $H_s$  bins' range is 0.25 m.

294 For these reasons, we now investigate alternative forcing fields for winds, ice  
 295 and currents, and their impact on the model results.

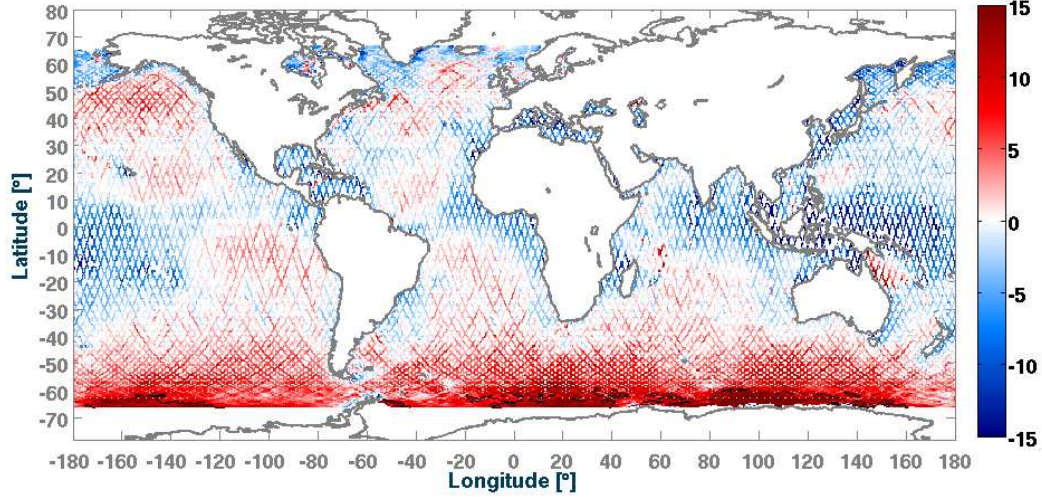


Figure 8: NMB for 1-year averaged  $H_s$  using ERA5 winds. Modelled year: 2011. Parameter settings from test T475. Colorbar indicates NMD values in %. Black lines represent positive 10 % contours.

### 3. Influence of forcing field choices

As we did for the choice of model parameters, forcing set-up and model adjustment was done over the year 2011, with a complete validation on other years described in section 6. Whereas we had used Jason-2 data only for the model calibration, we now use the full ESA Sea State Climate Change Initiative merged altimeter data set, using the denoised 1-Hz data for the significant wave height (Dodet et al., 2020). For the year 2011 this includes data from the following satellite missions: Jason-1, Envisat, Jason-2 and Cryosat-2. Using the model with parameters T475, our baseline model run uses ERA5 winds, Ifremer sea ice and iceberg concentrations, and CMES-Globcurrent surface currents.

#### 3.1. Choice of forcing wind field

We now look at three alternative wind fields. These include the operational ECMWF IFS winds which, for the year 2011, was obtained with IFS cycle 37r2, an earlier and less accurate version of IFS compared to the 41r2 used for ERA5. We also considered the CFSR winds (Saha et al., 2010) that were used by Raschle and Ardhuin (2013). Finally we tested the Ifremer CER-SAT Global Blended Mean Wind Fields (Bentamy et al., 2018), from here on just named "Ifremer". Other wind fields like ERA-Interim and MERRA2

315 (Gelaro et al., 2017) have also been considered in other hindcasts such as  
 316 Sharmar et al. (2021), with analyses focused on inconsistencies and trends of  
 317 the different atmospheric forcing.

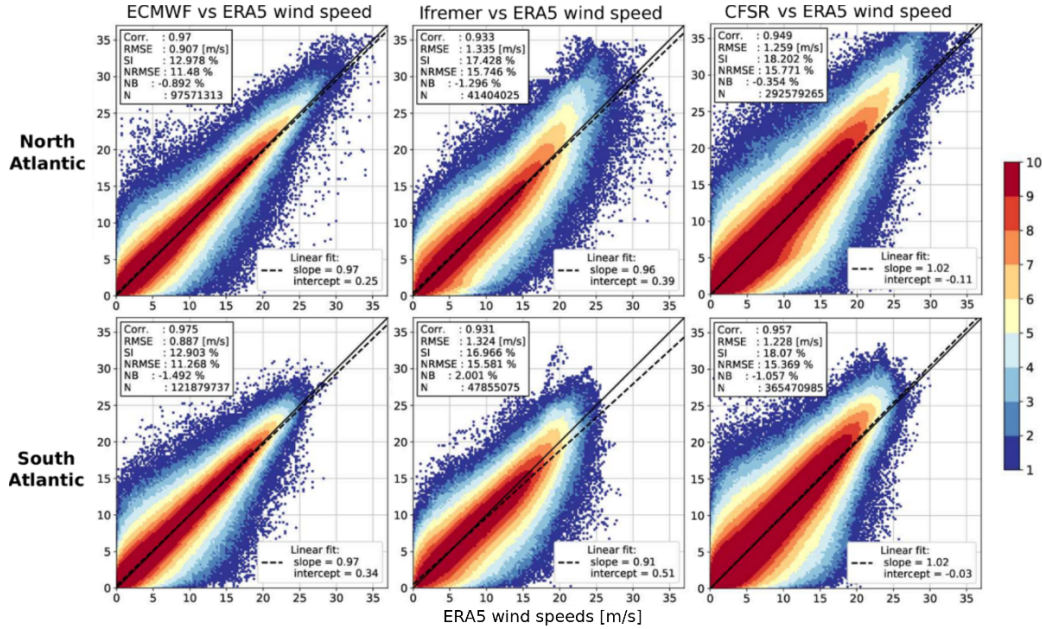


Figure 9: Scatter plot of wind speed for the months of January to July 2011. ERA5 intensity bins along x-axis. Top panels: ECMWF operational product vs ERA5, Middle panels: Ifremer vs ERA5. Bottom panels: CFSR vs ERA5. Colors give the logarithm of the number of data points in each 0.25 m/s×0.25 m/s wind speed bin.

318 The main difference between the Ifremer winds and the 2 other data sets,  
 319 is that the Ifremer 6-hourly surface wind fields are estimated mainly from  
 320 scatterometer wind vector observations, merged with wind magnitude mea-  
 321 surements from radiometer data (SSM/I, SSMIS, WindSat) and the ERA-  
 322 Interim atmospheric wind reanalyzes. Further details on the product and  
 323 methods can be found in Bentamy et al. (2012, 2013).

324 As discussed by Rasche and Ardhuin (2013) and Stopa et al. (2019), dif-  
 325 ferent wind fields are biased relative to one another. This is true for the  
 326 average values around 7 m/s, and biases are even larger for high speeds over  
 327 20 m/s (Pineau-Guillou et al., 2018). This is shown again here in Fig. 9.  
 328 The NCEP operational GFS model (not shown here) and CFSR hindcast  
 329 both have wind speeds higher than those produced by the ECMWF models  
 330 (operational IFS results and ERA5 results), leading to higher wave heights



when using NCEP winds. Because the Ifremer blended wind product uses ERA-Interim as a background "filler" when and where observations are too far in space or time, these data sets were homogenized to have the same low bias for average conditions (slope of 0.91 for the Ifremer wind vs the ERA5 winds in the South Atlantic) but higher values for wind speeds above 20 m/s that are more frequent in the North Atlantic.

There is also a clear indication that ECMWF operational winds give higher values for wind speeds above 20 m/s compared to ERA5, probably due to the higher resolution of the operational IFS model (25 km approx. and hourly output for 2011). The consequences of these wind field properties on the wave height biases are shown in Fig. 10.

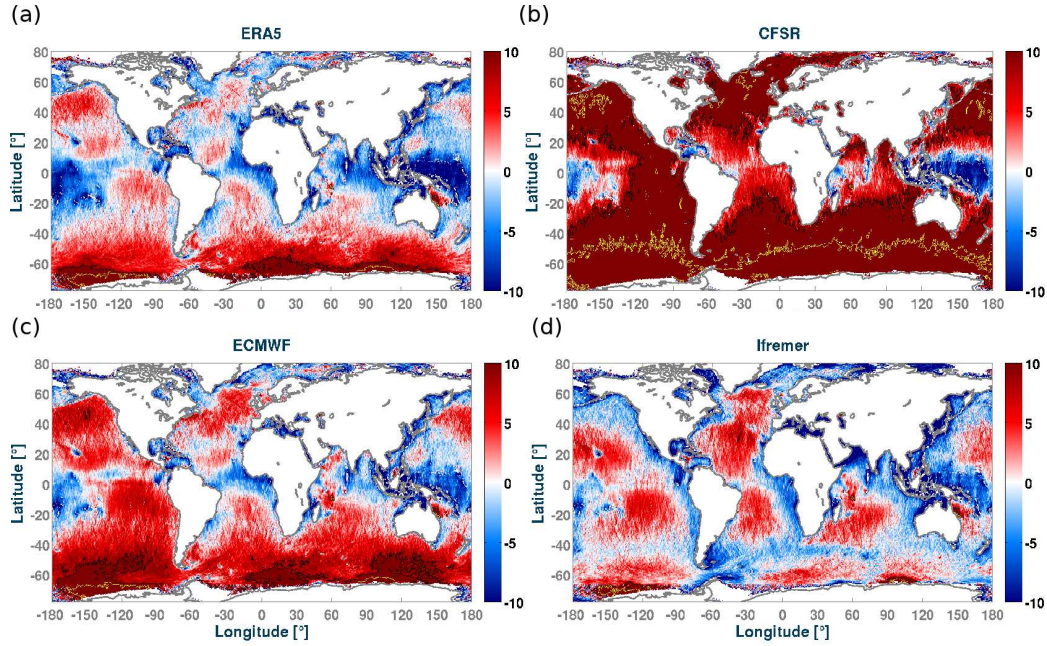


Figure 10: Normalized Mean Difference of modelled  $H_s$  minus Sea State CCI Altimeter data, averaged over the year 2011, using (a) ERA5, (b) CFSR, (c) ECMWF operational deterministic products and (d) Ifremer winds. The model was run with the set of parameters T475 as given in Table 2. Colorbar indicates NMD in percent. Black and yellow lines mark the +10 and +20 % contours.

Given the relative biases of the different wind datasets, it is not surprising that, without any retuning, the T475 set of parameters gives large  $H_s$  biases when used with other wind forcing than ERA-5. In particular the CFSR

345 winds give positive biases larger than 15% over most of the oceans.

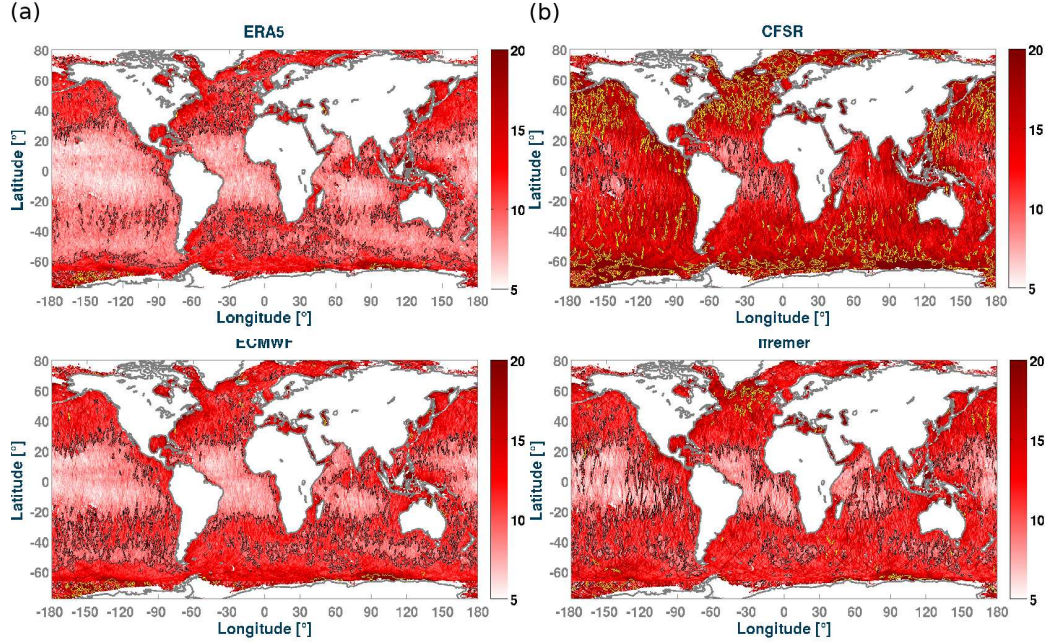


Figure 11: Scatter Index of modelled  $H_s$  minus Sea State CCI Altimeter data, averaged over the year 2011, using (a) ERA5, (b) CFSR, (c) ECMWF operational deterministic products and (d) Ifremer winds. The model was run with the set of parameters T475 as given in Table 2. Colorbar indicates SI in percent. Black and yellow lines mark the +10 and +20 % contours.

346 The Ifremer winds have interesting properties and are probably more  
 347 realistic in some regions, where they give lower scatter index (Fig 11.d),  
 348 including the southern ocean where the bias is also lower and significantly  
 349 different (Fig. 10.d). This difference between Ifremer and ERA5 winds is  
 350 possibly due to the fact that the remote sensing data used in the Ifremer  
 351 product generally measures a wind that is relative to the current and not an  
 352 absolute wind (Quilfen et al., 2004). There is also probably a contribution  
 353 to the generally low bias of the ERA-Iterim product that is used to fill in  
 354 between the different satellite passes.

### 355 3.2. Effects of wave-ice parametrizations and forcing fields

356 Much work has been done on the interactions of waves and sea ice in the  
 357 recent years, with a large emphasis on pancake ice (Thomson et al., 2018),



358 that is particularly relevant near the ice edge and during the freeze-up period  
 359 (Doble et al., 2003). Here we have rather used a parameterization associated  
 360 to the presence of larger floes and their possible break-up induced by waves.  
 361 In particular the formulation we have used in our baseline simulation was  
 362 developed by Boutin et al. (2018) and adjusted by Ardhuin et al. (2020) to  
 363 2 months of waves measured in the sea ice of the Ross sea. That parame-  
 364 terization combines both wave scattering in sea ice with a wave-induced ice  
 365 break-up (IS2) and dissipation below ice plates including a smooth laminar  
 366 to rough turbulent flow as a function of the boundary layer Reynolds number  
 367 (IC2, Stopa et al., 2016b). Given uncertainties on ice thickness, in partic-  
 368 ular in the Southern Ocean (Williams et al., 2014) and around the ice edge  
 369 where it matters for wave-ice interactions, we have chosen a crude and sim-  
 370 ple constant thickness of 1 m. This parameterization is compared to the old  
 371 default WW3 parameterization that is a 40 km exponential decay of wave  
 372 energy proportional to the ice concentration (IC0 parameterization). The  
 373 new IC2+IS2 parameterization gives a much weaker attenuation near the ice  
 374 edge, and thus a larger value of  $H_s$  in the open ocean where we have data  
 375 for validation (Fig. 12a,b). We have not attempted to validate the predicted  
 376 wave parameter and maximum floe size in the ice-covered regions. We note  
 377 that the scatter index is generally reduced around the ice, especially around  
 378 Greenland and in the Ross sea. These areas typically require more valida-  
 379 tion, and the model resolution ( $0.5^\circ$ ) is probably marginal for the Southern  
 380 Ocean, whereas the 12 km resolution in the Arctic allows a more detailed  
 381 investigation of wave-ice interactions.

382 Much less work has been devoted to the effect of icebergs, so we use  
 383 here the parameterization proposed by Ardhuin et al. (2011). We verify that  
 384 including icebergs has a very positive effect on reducing the bias and scatter  
 385 index where the icebergs are present. For the year 2011, a large concentration  
 386 of icebergs was found in both the South-East of the Pacific and the South  
 387 of the Indian ocean, giving a bias reduction up to 10 percentage points and,  
 388 locally, a very large reduction in scatter index up to 6 percentage points  
 389 (Fig. 12c,d). The concentration of icebergs in the South Pacific in 2011 is  
 390 associated with two large icebergs, C19a and B15j, that drifted northward  
 391 and eastward within the Antarctic Circumpolar Current (Tournadre et al.,  
 392 2015, 2016), later breaking up into hundreds of smaller icebergs. These small  
 393 icebergs are much more effective in reducing the wave energy flux, compared  
 394 to a single parent iceberg, as they have a much larger cross section.

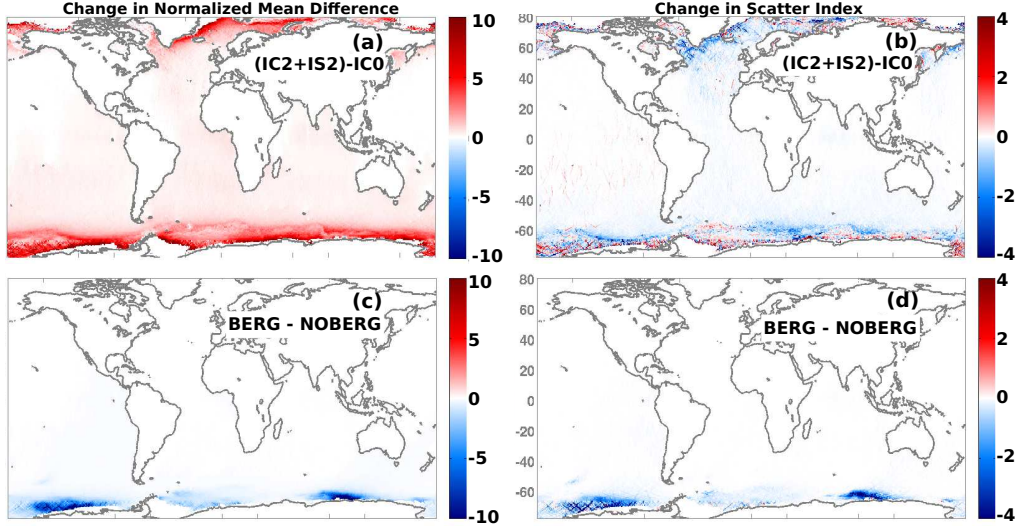


Figure 12: (a,b) using dissipation, scattering and ice break-up (IC2, IS2) or partial ice blocking (IC0) Differences in NMB and SI in percentage points for the T475 parameterization variations when using: (c,d) iceberg forcing or no iceberg forcing.

### 3.3. Effect of currents

Ocean surface currents can have large influences on the wave field either locally through the relative wind effect and advection, or down-wave of current gradients, due to refraction, with larger effects associated to larger current magnitude (Ardhuin et al., 2012). An important difficulty for properly taking currents into account at global scales is that there are no global observations of the Total Surface Current Velocity (TSCV) that matters for wind waves, and the only proper surface measurements are made with High Frequency radar near the coasts (Barrick et al., 1974; Roarty et al., 2019). Instead, the closest global proxy is given by the drift velocity around 15 m depth provided by instruments of the Surface Velocity Program (Elipot et al., 2016; Lumpkin et al., 2017), with only about 1500 drifters globally giving a 500 km resolution. We note that at the Equator and a few other places of interest, the 15-m depth drift is often in the opposite direction of the surface drift. Most importantly, finer spatial resolution is needed, typically down to 30 km, to represent most of the refraction effects (Ardhuin et al., 2017a; Marechal and Ardhuin, 2020). As a result, surface current estimates are often taken from numerical models, or, which is the case of the CMEMS Globcurrent product used here, derived from combined obser-

414 vations of sea surface height anomaly, mean dynamic topography and surface  
 415 winds, assuming a quasi-geostrophic equilibrium of the Coriolis force asso-  
 416 ciated to the surface current with the combination of the wind stress and  
 417 the pressure gradient associated to sea surface height. Except possibly for  
 418 western boundary currents such as the Gulf Stream or the Agulhas, this ap-  
 419 proach does not work very well, in particular around the equator and in mid-  
 420 latitudes where currents are dominated by near-inertial currents as illustrated  
 in Fig. 13. The CMEMS Global Ocean Multi Observation Products (MUL-

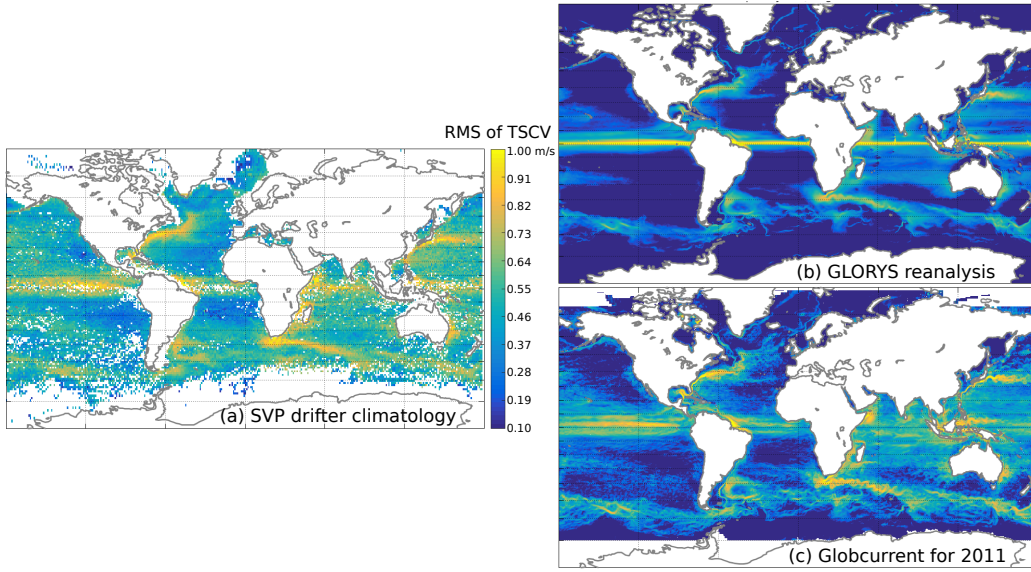


Figure 13: Root mean square current velocity (a) at 15 m depth using in situ drifter  
 data from the Surface Velocity Program (SVP) processed by Elipot et al. (2016) with  
 rms velocity computed over 30-day long trajectories and attributed to the center of that  
 trajectory and white ocean pixels corresponding to 1 by 1 degree squares in which no  
 data was available, (b) as given by the CMEMS GLORYS reanalysis, (c) as given by  
 the CMEMS-Globcurrent product based on altimeter sea level anomalies, mean dynamic  
 topography inferred from satellite gravimeters and ocean drifters, and "Ekman currents"  
 estimated from ECMWF wind analyses.

421 TIOBS.GLO.PHY.REP\_015\_004) has an average current that is closer to the  
 422 SVP drifter climatology than the CMEMS Global Ocean Reanalysis (GLO-  
 423 RYS) product GLOBAL-REANALYSIS-PHY-001-031, in particular around  
 424 the Equator, which is why we have chosen to use the former product as our  
 425 TSCV forcing.

427 Given all these limitations it is not specially surprising that the TSCV is

seldom used at global scale. Including the TSCV forcing can indeed increase errors in some regions due to errors in the forcing field, but it generally corrects part of the bias and gives lower scatter index for wave heights compared to altimeter data, as illustrated in Fig. 14. Comparing our simulation with parameters T475 with and without currents, we find a clear lower bias along the Equator and in the Southern ocean when currents are used, as already reported by Rascle et al. (2008). This is probably associated with the relative wind effect, with wave generation given by the difference between the wind vector and the TSCV and not the wind vector alone. We know that this approach can overestimate the current effect when the atmosphere model is not coupled with an ocean model (Hersbach and Bidlot, 2008; Renault et al., 2016), however, we also expect that the TSCV is generally underestimated by the CMEMS-Globcurrent product.

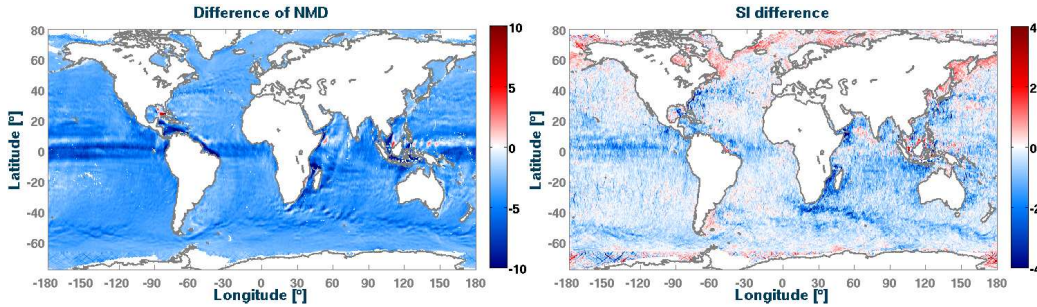


Figure 14: Left: Change in Normalized Mean Difference (NMD in percentage points) for  $H_s$  with currents and the T475 parameterization versus the same simulation without current. For both simulations the reference is the Sea State CCI  $H_s$  for the year 2011. Right: same for difference in SI, with the dark blue corresponding to a reduction of 4 percentage points (e.g. from 14% to 10%) when TSCV forcing is used.

The reduction of the scatter index against altimeter  $H_s$  that is brought by the current (blue regions in Fig. 14.b) clearly corresponds to the regions of strong currents where the variability of incoming waves can cause a large variability of the wave heights around the current: this is the case in the Agulhas current, in the Gulf Stream, the Kuroshio, the Mozambique channel, the Somali current. However, as shown in Fig. 11, these regions are still places where the models error are relatively large, possibly due to a combination of factors, including errors in the TSCV fields, insufficient directional resolution of our wave model (Marechal and Ardhuin, 2020), and insufficient spatial resolution in the TSCV field and/or the wave model. We note that

the scatter index is generally increased for latitudes above  $50^\circ$  N, probably due to an insufficient resolution of the altimetry where the Rossby radius of deformation is less than 50 km (Ballarotta et al., 2019). Given the importance of the spectral and spatial discretizations, we now discuss these aspects.

## 4. Model discretization

The choice of spatial and spectral discretizations can have a large impact on the model solutions, and it also has a direct and clear impact on the cost of the model, the time needed to perform the simulations. As a result, the particular choices we made for the discretizations are a compromise between the computational cost and the accuracy benefits. The 28-years hindcast used around 500,000 cpu hours distributed over 504 processors, distributed in 18 nodes that each hold 28 CPUs and 75Gb of memory.

### 4.1. Spatial resolution

Using higher resolution grids is critical for resolving smaller scale variations in the sea state that are caused by the time-varying forcing fields (wind, current, sea ice) or fixed features (shoreline, water depth, bottom sediment type and grain size). In practice, small scale gradients in wave heights are dominated by the distance to the coast and the presence of strong currents (Quilfen and Chapron, 2019). Because some important current system are located close to coasts, we have chosen to define nested grids that cover the relatively shallow waters of the coastal regions and, where possible, extend over strong current regions (Fig. 1). As a result, our North-West Atlantic grid covers the Grand Banks and the Gulf Stream, as well as the entire gulf of Mexico. In a similar fashion, the Africa grid was extended to the south to cover the Agulhas current retroflexion. Using different grids also allows to tune the model parameters locally.

Because the wind-wave growth tuning that corresponds to T475 is very similar to T471, it tends to give an underestimation of the wave height for short fetches (Stopa et al., 2016a). This effect is more pronounced with higher resolution grids, which explains the general reduction in wave height for enclosed seas and eastern coasts (stronger negative bias, in blue in Fig. 15.a). We also find that the explicit higher resolution of shorelines and islands gives larger  $H_s$  values compared to the subgrid treatment of complex shorelines and islands in a coarser grid (Chawla and Tolman, 2008), explaining the more



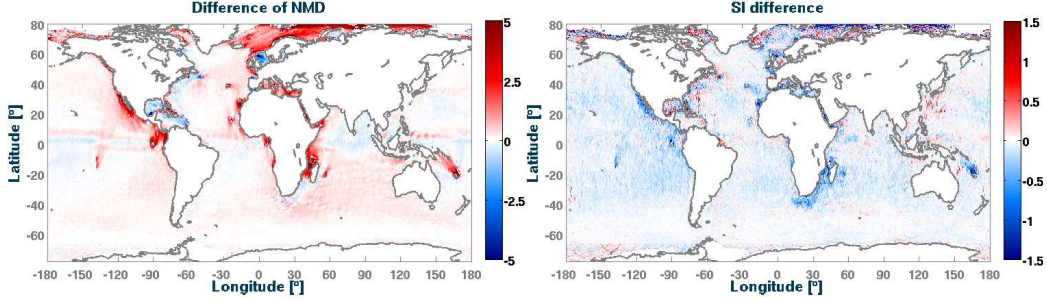


Figure 15: NMD and SI variations in percentage points for the year 2011: values for Multi-grid minus values for Single grid setup, both using the same T475 parameters. Left panel: Difference in NMD values, in this case red values represent a reduction of the negative NMD.

positive bias around 140E 10S, downwave of the Tuamotus, or around the Galapagos, Azores etc. The presence of the full Arctic ocean thanks to the Arctic grid also adds wave energy that was otherwise missing in the near-global grid that stopped at 83°N.

Overall, the scatter index is reduced over most of the ocean with the strongest reduction in regions of strong currents like the Agulhas current, or along complex coastlines such as the Baja California peninsula (blue regions in Fig. 15.b).

#### 4.2. Spectral grid and resolution

However, to converge to the true solution of the wave action equation, increasing only the spatial resolution is not enough, and a finer spectral resolution is also needed, in particular for parameters sensitive to numerical diffusion like the directional spread (Ardhuin and Herbers, 2005). Although we know that current effects on wave heights would be better resolved with 48 directions instead of only 24 (Ardhuin et al., 2017b; Marechal and Ardhuin, 2020), we have stuck to 24 directions only because of the much lower CPU cost, and because differences in wave heights when using 24 or 36 directions were fairly limited. Fig. 16.b shows a change in the Normalized Mean Difference that is mostly limited to the tropical regions, especially around coasts and islands for which the finer directional resolution must have an impact on swell propagation, but the change in scatter index is typically much less than 1 percentage point (Fig. 16.d).

Compared to the costly increase of directional resolution, we found a higher benefit in terms of  $H_s$  accuracy in increasing the spectral range with

510 a maximum frequency of 0.95 Hz instead of the 0.72 Hz used by [Raschle and](#)  
511 [Ardhuin \(2013\)](#). This higher frequency gives a better response, in particular  
512 for the short fetch and low wind conditions in which the peak of the wind  
513 sea would otherwise not be well resolved.

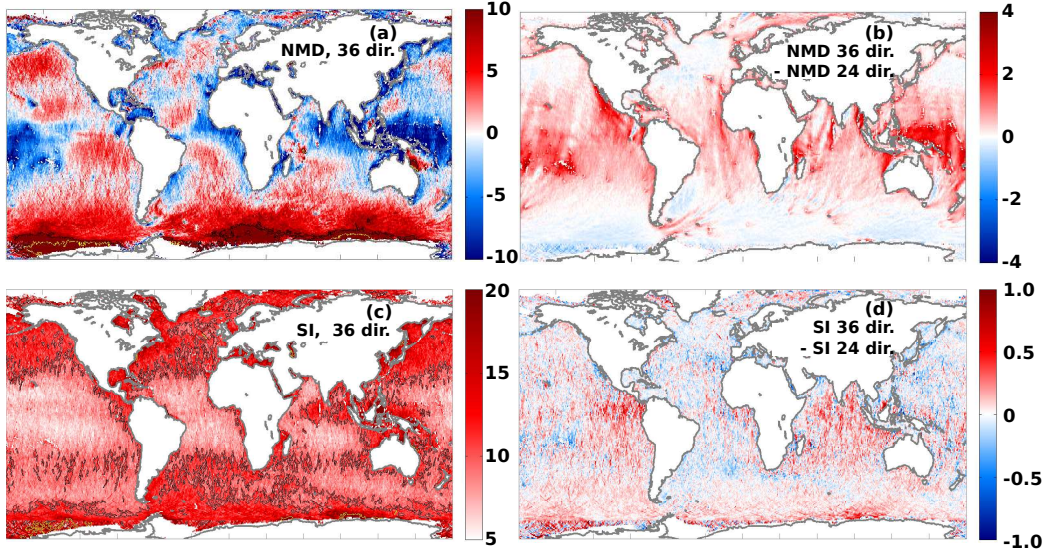


Figure 16: (a)NMD for 1 year averaged  $H_s$  using T475 with 36 directions and (b) differences in NMD for T475 with 36 directions with respect to 24 directions (Fig. 10a). Black lines mark the positive 10 % contours. (c) SI for 1 year averaged  $H_s$  using T475 with 36 directions and (d) SI difference for T475 with 36 directions with respect to 24 directions. Analyzed year: 2011. Black and yellow lines mark the positive 10 and 20 % contours respectively

## 514 5. Wave directionality and alternative dissipation parameteriza- 515 tions

516 As noted by [Stopa et al. \(2016b\)](#), the directional spread ([Kuik et al.,](#)  
517 [1988](#)) is the least well predicted parameter among the most common metrics  
518 used to define the shape of the wave spectrum. Whereas the mean direction  
519 is well controlled by the wind evolution and the time scale of adjustment  
520 of the wave field, the directional spread is probably influenced by details  
521 of the wave generation and dissipation parameterizations. Here we use 3-  
522 hour averaged data from WMO buoy 46436 in the North East Pacific as an  
523 example (see table 4 and Fig. 17), which is the station 166 of the Coastal

524 Data Information Program and is maintained by Thomson et al. (2013). The  
 525 correlation coefficient for  $\sigma_\theta(f)$  falls below 0.7 for frequency above 0.3 Hz.  
 526 Indeed, the model has no skill in predicting  $\sigma_\theta(f)$  for  $f > 0.5$  Hz, and the  
 527 shape of the modeled spectral tail is given by the shape at frequency  $f_m$  with  
 528 an energy level decreasing like  $(f_m/f)^5$ , where  $f_m$  is a dynamically adjusted  
 529 maximum prognostic frequency, set to 2.5 times the mean frequency of the  
 530 wind sea part of the spectrum.

531 We note that the directional spread at low frequencies is, close to coasts,  
 532 very sensitive to shoreline reflections (Ardhuin and Roland, 2012). Whereas  
 533 this has a limited impact on most wave parameters, it is a critical contribution  
 534 to microseism and microbarom sources (Stutzmann et al., 2012; De Carlo  
 535 et al., 2021). In the present hindcast we have not used the slope-based  
 536 reflection coefficient proposed by Ardhuin and Roland (2012) because of the  
 537 difficulty of defining the proper slope and mixed results when validating  
 538 modeled microseisms. Instead, we have used constant reflexion coefficients of  
 539 5%, 10% and 20% for the resolved shorelines, subgrid shorelines and icebergs,  
 540 respectively. Clearly that parameterization will have to be tested and further  
 541 improved upon using buoy directional spreads together with microseism and  
 542 microbarom data.

543 The T475 parameterization is thus still fairly poor for the frequency range  
 544 0.4 to 1 Hz when the waves are developed (when the wind sea peak frequency  
 545 is below 0.15 Hz), in particular for the directional distribution (Fig. 17.d),  
 546 which is critical for the ratio of crosswind to downwind mean square slope  
 547 (Munk, 2009), wave breaking statistics (Romero et al., 2017) and the sources  
 548 of microseisms and microbaroms at seismic or acoustic frequencies above  
 549 0.8 Hz (Farrell and Munk, 2010; Peureux and Ardhuin, 2016; De Carlo et al.,  
 550 2020). Recent work have suggested that the shape of the dissipation func-  
 551 tion could be better described by Romero (2019), giving the T700 set of  
 552 parameters in the WAVEWATCH III model, available in versions 7.0 and  
 553 above. In T700, the ad hoc and not very effective cumulative term of Ard-  
 554 huin et al. (2010) is replaced with a cumulative term that could be explained  
 555 by the straining of short waves caused by long waves (Peureux et al., 2020).  
 556 Preliminary tests reveal an interesting behavior for the shape of the high fre-  
 557 quency spectrum (Fig. 18), which allows to remove the imposed diagnostic  
 558 tail for  $f > f_m$  thanks to a completely local (in the spectral sense) param-  
 559 eterization of the breaking probability, and the added cosine-squared angular  
 560 dependence in the parameterization of the cumulative effect. Possibly this  
 561 imposed shape of the cumulative term will have to be revised, as for example



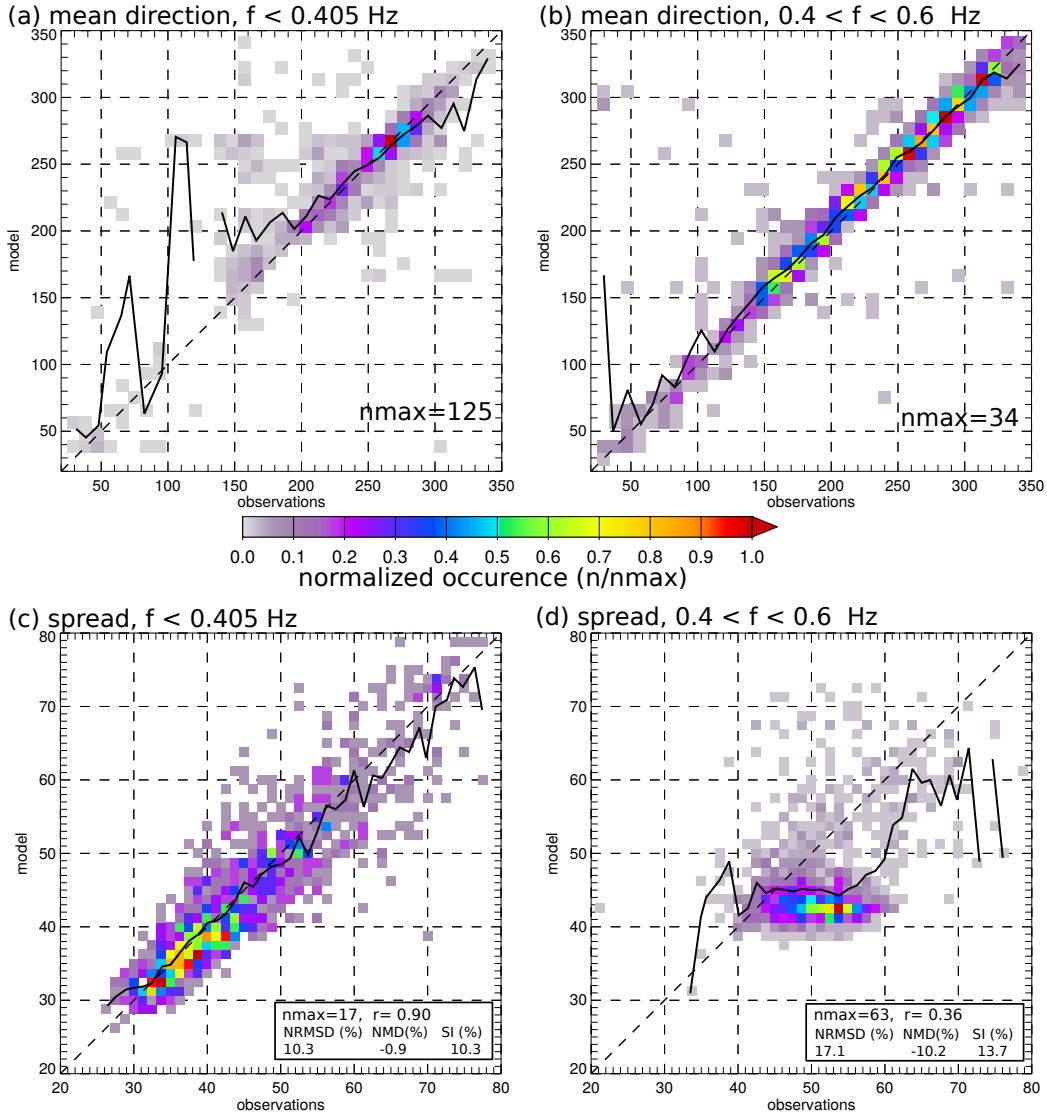


Figure 17: Modeled spread and mean direction for low frequencies ( $f < 0.4$  Hz) and high frequencies ( $f > 0.4$  Hz) at buoy 46246 for the year 2018. Colors show the number of 3 hour records for which the model-buoy pair falls in one bin, as normalized by the maximum value  $n_{\max}$ . The solid lines gives the mean modeled value for each observation bin.

562 an isotropic spectrum of long waves should produce an isotropic effect unless  
 563 it is a joint effect of the long and short waves. However, [Romero \(2019\)](#) has  
 564 produced the first parameterization that is able to produce larger cross-wind

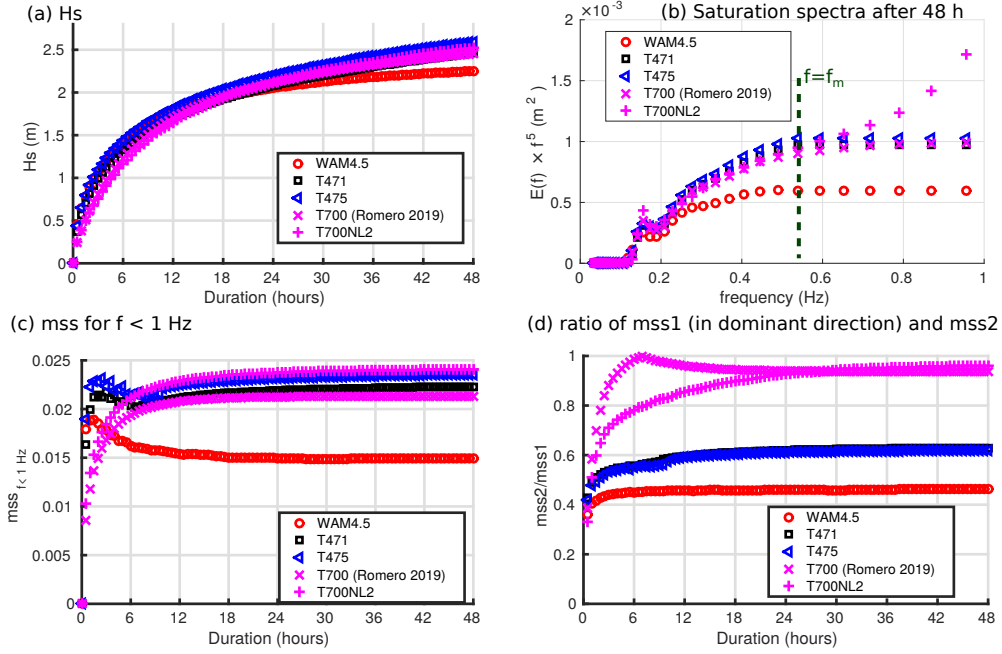


Figure 18: Differences in model results for an academic case considering a uniform ocean and a constant wind speed of 10 m/s starting from no waves. The WAM4.5 parameterization is close to the one used in the ERA5 reanalysis, and the T700NL2 corresponds to the parameterization of Romero (2019) with the non-linear interactions computed with the exact Webb-Resio-Tracy method [van Vledder \(2006\)](#).

565 slopes than down-wind slopes for wavelengths around 1 m (after 7 hours in  
 566 Fig. 18.d, the dominant direction for mss1 in T700NL2 is indeed the cross-  
 567 wind direction), which are critical to explain the first of the inconvenient sea  
 568 truths highlighted by [Munk \(2009\)](#).

569 Taken "out of the box" without the present retuning, the [Romero \(2019\)](#)  
 570 parameterization performs similarly to T471 in terms of scatter index but  
 571 has a 2 to 6% higher value of wave height (Fig. 19) that will also require an  
 572 adjustment of the swell dissipation. The benefits of such a parameterization  
 573 will probably be most important for the model parameters that are most  
 574 sensitive to the high frequencies, including the mean square slope, and will  
 575 require an important upgrade of the wave model in the way these shorter  
 576 wave components are treated, so that the wave model result can be validated  
 577 with radar back-scatter data (e.g. [Nouguier et al., 2016](#)). This effort is beyond  
 578 the scope of the present paper and will be discussed in Part 4.

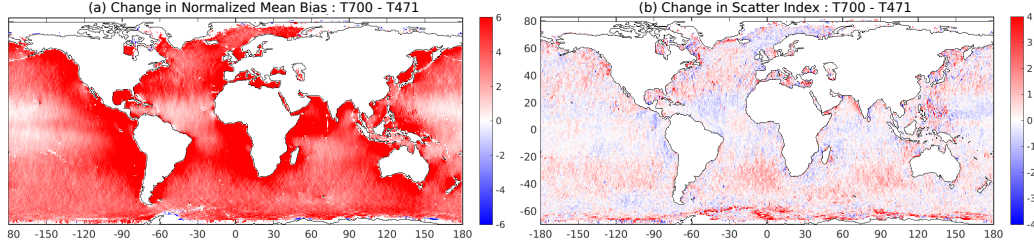


Figure 19: Change in NB and SI from the T471 to T700 change in parameterization for the year 2018. These simulations did not include ocean currents.

## 6. Validation

### 6.1. Validation with altimeter data

An important concern about numerical wave model hindcasts for all applications is their consistency in time which can be compromised by the time-evolving error statistics of the forcing fields (winds, currents, sea ice) and/or of the assimilated data which may both introduce time varying biases and jumps, possibly requiring the statistical adjustment of the forcing fields (e.g. [Stopa et al., 2019](#)) or the correction of the model results. It is thus necessary to verify the consistency of the model output over time. This requires validation data that are stable in time. Here we use the satellite altimeter  $H_s$  measurements of [Dodet et al. \(2020\)](#) that were especially designed for this purpose, and we look at the evolution of the NMB and SI over the years 1997 to 2018 (Fig. 20). We find a general agreement over the years, with lower variations of the mean difference than was found by [Rascle and Ardhuin \(2013\)](#) when using CFSR winds, and which had to be corrected in later hindcasts ([Stopa et al., 2019](#)). Still, the changes from -1 to 2% for the bulk of the data ( $1.5 < H_s < 4$  m) suggest a systematic drift in either the ERA5 wind speeds or the altimeter data, with relatively flatter biases as a function of  $H_s$  for the years 2011-2018 (but still a decrease in the mean model values or an increase in the altimeter values), and steeper  $H_s$ -dependent biases for the years 1997-2010. The scatter index shows a general reduction of the random differences that can be caused by a reduction in the random noise of satellite altimeter data for the more recent missions and an improvement in the quality of the ERA5 wind fields thanks to the assimilation of a richer set of data ([Hersbach et al., 2020](#)).

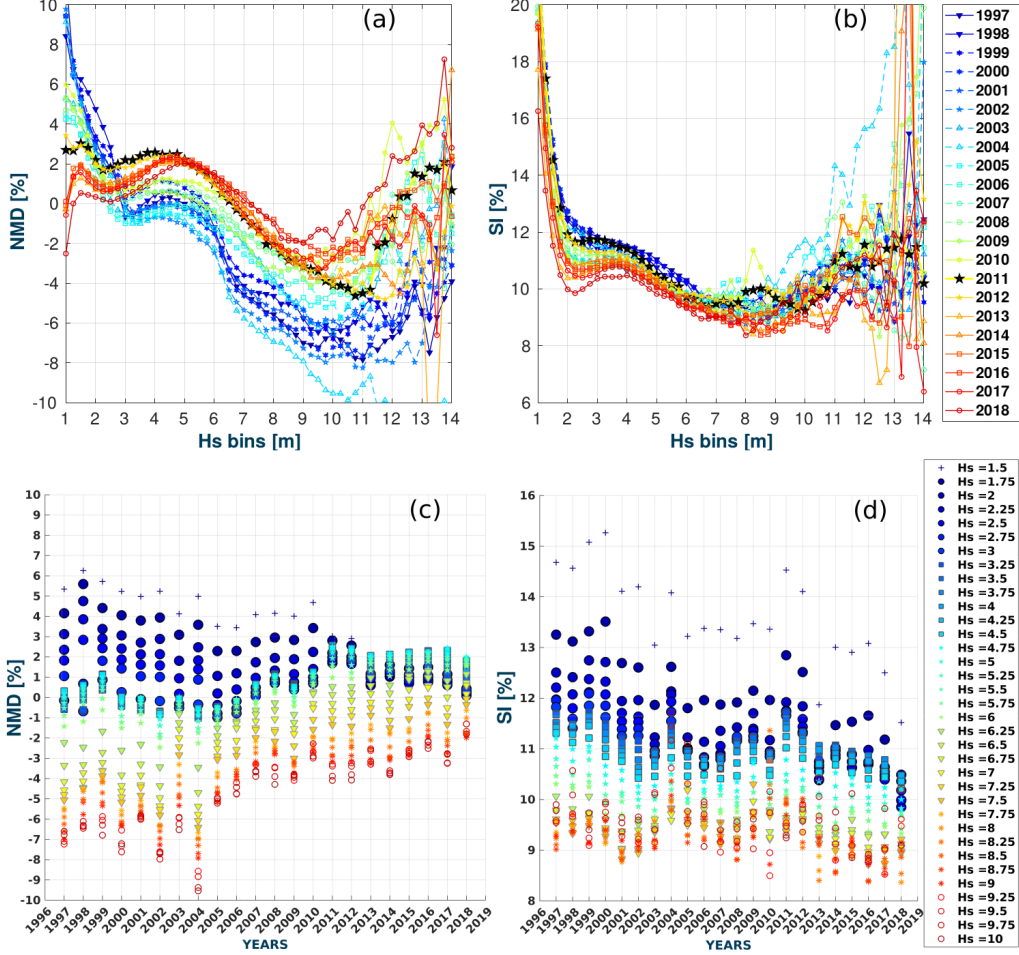


Figure 20: Performance parameters for 22 years hindcast using T475. (a)  $H_s$  NMD curves and (b) SI curves, the reference year (2011) used for model tuning has been highlighted with a black star. (c) and (d) are the NMD and SI time series of 1.5 to 10 m  $H_s$  bins. Bin size is 0.25 m. Altimeters used for validation: Topex (1997-2002), Envisat (2003-2010), Jason-2 (2011-2012), Saral (2013-2018).

## 6.2. Comparison to ERA5 wave heights

Because the ERA5 reanalysis also included a wave model it is questionable that our efforts have any added value, especially because the ERA5 wave model assimilates altimeter wave heights and uses a wind forcing at the 10 minutes time step of the atmospheric circulation model to which it is coupled. However, we know (J.R. Bidlot, personal communication) that the same

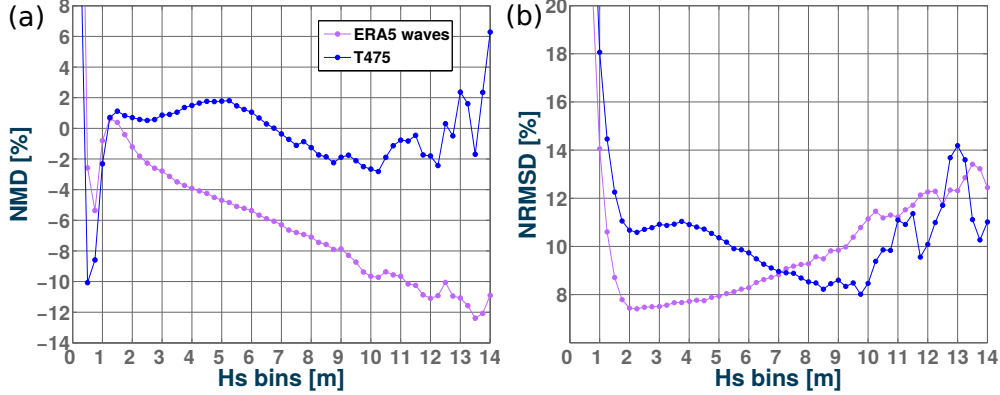


Figure 21: Performance parameters curves for test T475 and ERA5 wave product with respect to Jason-3 altimeter data. (a)  $H_s$  NMD, and (b) NRMSD. Analyzed year: 2018.  $H_s$  bin size is 0.25 m.

ECMWF wave model that uses improved wave generation and dissipation parameterization in the IFS cycle 46R1 that is operational as of June 6, 2019 (ECMWF, 2019) and is similar to T471, already gives better results than the ERA5 wave heights at buoy locations. It is thus interesting to look at the differences between the ERA5 wave heights and the results of the present hindcast. We note that our model uses different forcing, in particular for currents, sea ice and icebergs, includes some shoreline and iceberg reflexion and produces different output parameters, including fluxes of energy between the ocean and atmosphere, in addition to the parameters that can be derived from the wave spectrum. Here we only compare the two simulations using the Jason-3 data for 2018, which has not been assimilated in ERA5.

Fig. 21 shows a very strong negative bias in the ERA5 wave heights that, combined with a much lower random errors, gives larger rms differences for  $H_s > 7$  m. Looking at the spatial distribution of these errors we typically find larger random errors in the Southern ocean with T475 compared to ERA5 wave heights (Fig. 22), possibly a benefit of the assimilation of the other satellite missions where the satellite tracks are most dense, and we find lower random error in a few specific areas with T475, including in the Agulhas current, which shows again the benefit of properly including ocean surface currents in a wave model.

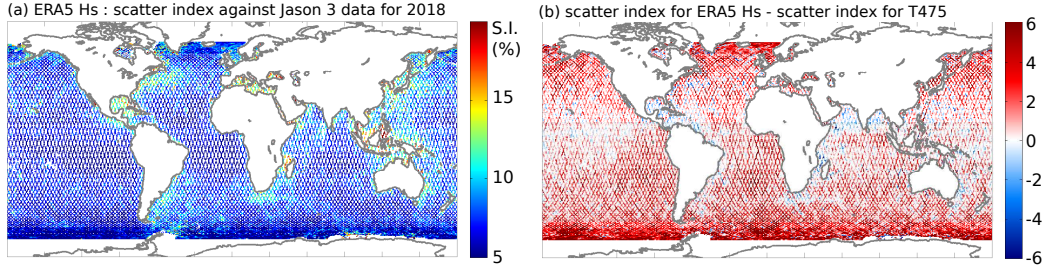


Figure 22: (a) Scatter Index for 1 year (2018) averaged ERA-5  $H_s$  with respect to Jason-3 altimeter data. (b) Difference in scatter index between T475 and ERA-5 waves product.

### 6.3. Validation with buoy data

So far all of our analysis, except for a brief discussion of mean direction and directional spread, has been based on wave heights alone, whereas our model hindcast is based on the simulation of ocean wave spectra and produces a wide range of spatially gridded parameters as well as spectra at selected locations: around 10,000 points all along the world coastline plus the locations of moored buoys and a few additional offshore points. Even though the model was only marginally changed compared to the version validated by [Stopa et al. \(2016a\)](#), it is interesting to look at errors on the shape of spectra and wave period and directions parameters.

These comparisons are not simple because of the large response differences of different buoy types for wavelengths shorter than 10 m ( $f \simeq 0.4$  Hz) in particular 3 m diameter discus buoys tend to filter frequencies above 0.4 Hz which are well reproduced, up to 0.6 Hz by 0.8 m diameter Waverider buoys (e.g. [Ardhuin et al., 2019](#)). We thus focus on the 0.05 to 0.4 Hz frequency band. Another difficulty is that most Waverider buoys are located in coastal areas. We have particularly selected 5 buoys that are representative of different wave climates, as listed in Table 4. The buoy heave spectra were averaged over 3 h intervals.

Fig. 23 shows different validations of the spectral content of the wave spectrum. Away from the coasts, at station Papa (buoy 46246), the average wave spectra in Fig. 23.a reveal a general good behavior of the model compared to Datawell buoy measurements with mean differences under 10% in the frequency range 0.05 to 0.4 Hz. The deviation at low frequencies can be due to the presence of infragravity waves in the buoy measurements which were not included in our model simulation, but could have been added and have a typical height of 1 cm in the open ocean ([Ardhuin et al., 2014](#)). That

WMO code	latitude	longitude	depth	shore distance	buoy type
46246	50.0N	145.2 W	4252 m	900 km	Datawell WR
51208	22.285 N	159.574 W	200 m	5 km	Datawell WR
51004	17.53 N	152.25 W	5183 m	300 km	3-m discus
42097	25.7 N	83.65 W	81 m	130 km	Datawell WR
44098	42.8 N	70.17 W	77 m	37 km	Datawell WR

Table 4: List of buoys selected for detailed validation over the years 2018 and 2019. Note that data was missing before July 6, 2019 for buoy 46246.

657 deviation could also be the result of mooring line effects. At high frequen-  
658 cies, the model underestimation for  $f > 0.5$  Hz may be due to the buoy heave  
659 resonance (Datawell, 2014).

660 The variability of the energy content at different frequencies is generally  
661 well captured by the parameters  $H_s$  and mean periods  $T_{m0,2}$  (which is more  
662 sensitive to the high frequencies) and  $T_{m-1,0}$  (more sensitive to the low fre-  
663 quencies). With a bias for the mean periods at buoy 46246 under 1% and a  
664 scatter index around 5%, the model is particularly accurate for the shape of  
665 the wave spectrum.

666 For other buoys, differences between the model and the observations can  
667 reveal errors in buoy measurements (e.g. the spectrum roll-off for  $f > 0.52$  Hz  
668 at 51004 is typical of 3-m discus buoys) and difficulties for the model to re-  
669 solve coastal sea state variability and growth for relatively short fetches. In  
670 particular, the energy for low frequencies ( $f < 0.06$  Hz) is strongly underes-  
671 timated in the Gulf of Mexico and the Gulf of Maine.



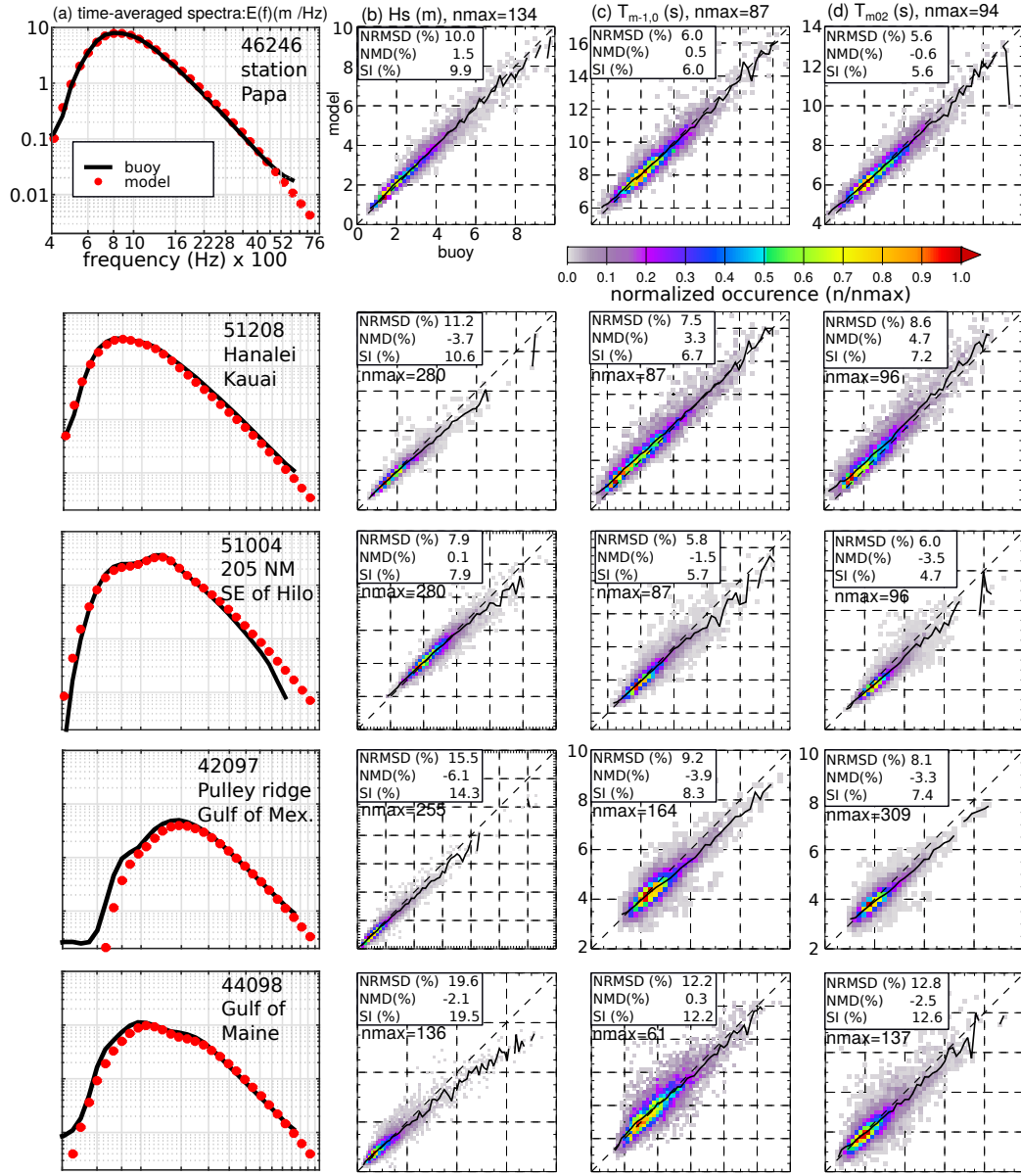


Figure 23: Modeled and measured mean spectra, scatter plots for  $H_s$ , and mean periods  $T_{m-1,0}$ ,  $T_{m0,2}$  at selected buoys listed in Table 4.



## 672 7. Conclusions

673 The present paper discusses the influence of forcing fields (winds, sur-  
 674 face current, sea ice concentration, iceberg concentration), parameterizations  
 675 (wind-wave generation and swell damping) and resolution (in physical and  
 676 spectral space) on the wave heights produced by a wave model hindcast, us-  
 677 ing the WAVEWATCH III modelling framework and satellite-derived wave  
 678 heights. It is unfortunately not practical to test all the possible combina-  
 679 tions of model settings, but we expect that the choice of forcing fields and  
 680 adjustment of parameters is generally robust, and the measurements shows  
 681 that the present hindcast, in the context of the Integrated Ocean Waves for  
 682 Geophysical and other Applications (IOWAGA) project, is generally supe-  
 683 rior to the previous version described by [Raschle and Ardhuin \(2013\)](#), and in  
 684 some regions, for large wave heights, is superior to the ERA5 reanalysis wave  
 685 product.

686 For the forcing, we found that ERA5 winds, once corrected for a low bias  
 687 at wind speeds above 21 m/s, gave more accurate results than operational  
 688 ECMWF analyses or the CFSR reanalysis. Alternative merged satellite-  
 689 model products ([Bentamy et al., 2018](#)) gave interesting results. We also  
 690 found that the use of currents provided by CMEMS-Globcurrent generally  
 691 improved the model results. Probably because these current estimates are  
 692 missing a significant part of the Total Surface Current Velocity, they degraded  
 693 the model results at latitudes larger than 50° N. Finally, we confirmed the  
 694 importance of both sea ice and icebergs for Southern Ocean and Arctic wave  
 695 heights.

696 For the model parameterizations of air-sea interactions, we have shown  
 697 that the distribution of  $H_s$  around the global maximum of 2 m, could be  
 698 used to adjust the transition from a laminar to a turbulent boundary layers  
 699 above the waves, that is very important for the attenuation of swells, and is  
 700 probably the most sensitive part of the model parameterizations.

701 Regarding model discretizations, we have found a great benefit in includ-  
 702 ing the 0.7 to 1 Hz frequency range, even though the directionality in that  
 703 range is not yet well described by the model when waves are developed.

704 For all these tests, we have only performed limited validation for other  
 705 parameters besides the significant wave height. We expect that future adjust-  
 706 ments will particularly focus on the high frequencies ( $f > 0.4$  Hz) with more  
 707 validation of the variables that are most sensitive to that frequency range,  
 708 starting with the mean square slope and its directional components. In this

709 respect, we expect to produce a Part 4 update on the present work based on  
 710 the parameterizations of [Romero \(2019\)](#) and a much better treatment of the  
 711 model high frequencies that would make it consistent with remote sensing  
 712 data, as analyzed by [Nouguier et al. \(2016\)](#) or [Yueh et al. \(2006\)](#), following  
 713 the work of [Elfouhaily et al. \(1997\)](#).

## 714 Acknowledgments

715 The present work was supported by ESA Climate Change Initiative Pro-  
 716 gram, EU ERANET Resourcecode and CNES. Buoy data were furnished by  
 717 the Coastal Data Information Program (CDIP), Integrative Oceanography  
 718 Division, operated by the Scripps Institution of Oceanography, under the  
 719 sponsorship of the U.S. Army Corps of Engineers and the California De-  
 720 partment of Parks and Recreation. <https://doi.org/10.18437/C7WC72>. We  
 721 are grateful to many colleagues, including Abderrahim Bentamy and Camille  
 722 Lique for many constructive discussions. The authors would like to thank to  
 723 the 4 anonymous reviewers who, through their comments and observations,  
 724 have helped to improve the quality of this manuscript.

## 725 Data availability

726 The generated hindcast using test T475, will be available in the following  
 727 web site: <https://www.umn-lops.fr/Donnees/Vagues/sextant>

728 At the moment of the generation of the present study, the wave data  
 729 set covers 28 years, from 1993 to 2020 with 3-hourly outputted data. The  
 730 extension of the hindcast to prior and more recent years is an ongoing work.

## 731 Appendix A. Detailed model implementation

732 The wave model hindcast and tests presented here all use version 7.0 of  
 733 WAVEWATCH III. The hindcast uses a list of switches, which appears in all  
 734 NetCDF file products,

- 735 • physical parameterizations : LN1 ST4 STAB0 NL1 BT4 DB1 MLIM
- 736 TR0 BS0 IC2 IS2 REF1 RWND WCOR
- 737 • advection and GSE correction: PR3 UQ

738 • other numerical aspects: F90 NOGRB NC4 SCRIP SCRIPNC DIST  
739 MPI FLX0 XX0 WNT2 WNX1 CRT1 CRX1 TIDE TRKNC O0 O1  
740 O2 O2a O2b O2c O3 O4 O5 O6 O7

741 The model parameters are adjusted with the same parameters for all  
742 model grids, and except for default parameter values the T475 parameters  
743 use these adjustments

744 • air-sea interaction parameters (SIN4 namelist) BETAMAX = 1.75,  
745 SWELLF = 0.66, TAUWSHELTER = 0.3, SWELLF3 = 0.022, SWELL-  
746 F4 = 115000.0, SWELLF7 = 432000.00

747 • wave-ice dissipation parameters (SIC2 namelist) IC2DISPER = F, IC2-  
748 TURB = 1.0, IC2ROUGH = 0.001, IC2DMAX = 0.3, IC2REYNOLDS  
749 = 150000, IC2SMOOTH = 200000., IC2VISC = 2.

750 • wave-ice scattering and floe size effects including break-up and in-  
751 elastic dissipation (SIS2 namelist): ISC1 = 0.2, IS2C2 = 0., IS2C3  
752 = 0., IS2BACKSCAT = 1., IS2BREAK = T, IS2DUPDATE = F,  
753 IS2CREEPB = 0.2E8, IS2CREEPD = 0.5, IS2CREEPN = 3.0, IS2-  
754 BREAKF = 3.6, IS2WIM1 = 1.0, IS2FLEXSTR = 2.7414E+05, IS2-  
755 CREEPC = 0.4, IS2ANDISE = 0.55

756 • reflexion parameters (REF1 namelist): REF Coast = 0.05, REF-  
757 COSP\_STRAIGHT = 4, REFFREQ = 1., REFICEBERG = 0.2, REF-  
758 MAP = 0., REFSLOPE=0., REFSUBGRID = 0.1, REFRMAX = 0.5

759 • other parameterizations (MISC namelist) ICEHINIT = 1., ICEHMIN  
760 = 0.1, CICE0 = 0.25, CICE1 = 2.00, LICE = 40000., FLAGTR = 4,  
761 FACBERG = 0.2, NOSW = 6, WCOR1 = 21., WCOR2 = 1.05 /

762 • activation of 3D output fields (full spectra and seismic sources, OUTS  
763 namelist) P2SF = 1, E3D = 1, I1P2SF = 3, I2P2SF = 24

## 764 References

765 Ardhuin, F., Chapron, B., Collard, F., 2009. Observation of swell dissipation  
766 across oceans. *Geophys. Res. Lett.* 36, L06607.

- 767 Ardhuin, F., Dumas, F., Bennis, A.-C., Roland, A., Sentchev, A., Forget,  
768 P., Wolf, J., Girard, F., Osuna, P., Benoit, M., 2012. Numerical wave  
769 modeling in conditions with strong currents: dissipation, refraction and  
770 relative wind. *J. Phys. Oceanogr.* 42, 2101–2120.
- 771 Ardhuin, F., Herbers, T. H. C., 2005. Numerical and physical diffusion: Can  
772 wave prediction models resolve directional spread? *J. Atmos. Ocean Tech-*  
773 *nol.* 22 (7), 886–895.  
774 URL <http://journals.ametsoc.org/doi/pdf/10.1175/JTECH1723.1>
- 775 Ardhuin, F., Otero, M., Merrifield, S., Grouazel, A., Terrill, E., 2020. Ice  
776 breakup controls dissipation of wind waves across southern ocean sea ice.  
777 *Geophys. Res. Lett.* 47, e2020GL087699.
- 778 Ardhuin, F., Raschle, N., Chapron, B., Gula, J., Molemaker, J., Gille, S. T.,  
779 Menemenlis, D., Rocha, C., 2017a. Small scale currents have large effects  
780 on wind wave heights. *J. Geophys. Res.* 122 (C6), 4500–4517.
- 781 Ardhuin, F., Rawat, A., Aucan, J., 2014. A numerical model for free in-  
782 fragravity waves: Definition and validation at regional and global scales.  
783 *Ocean Modelling* 77, 20–32.
- 784 Ardhuin, F., Rogers, E., Babanin, A., Filipot, J.-F., Magne, R., Roland, A.,  
785 van der Westhuysen, A., Queffelec, P., Lefevre, J.-M., Aouf, L., Collard,  
786 F., 2010. Semi-empirical dissipation source functions for wind-wave models:  
787 part I, definition, calibration and validation. *J. Phys. Oceanogr.* 40 (9),  
788 1917–1941.
- 789 Ardhuin, F., Roland, A., 2012. Coastal wave reflection, directional spreading,  
790 and seismo-acoustic noise sources. *J. Geophys. Res.* 117, C00J20.
- 791 Ardhuin, F., Stopa, J. E., Chapron, B., Collard, F., Husson, R., Jensen,  
792 R. E., Johannessen, J., Mouche, A., Passaro, M., Quartly, G. D., Swail,  
793 V., Young, I., 2019. Observing sea states. *Frontiers in Marine Sci.* 6, 124.
- 794 Ardhuin, F., Suzuki, N., McWilliams, J. C., Aiki, N., 2017b. Comments on  
795 “a combined derivation of the integrated and vertically resolved, coupled  
796 wave-current equations”. *J. Phys. Oceanogr.* 47 (9), 2377–2385.

797 Ardhuin, F., Tournadre, J., Queffelec, P., Girard-Ardhuin, F., 2011. Obser-  
798 vation and parameterization of small icebergs: drifting breakwaters in the  
799 southern ocean. *Ocean Modelling* 39, 405–410.

800 Ballarotta, M., Ubelmann, C., Pujol, M.-I., Taburet, G., Fournier, F., Leg-  
801 eais, J.-F., Faugere, Y., Delepouille, A., Chelton, D., Dibarboure, G., Picot,  
802 N., 2019. On the resolutions of ocean altimetry maps. *Ocean Science Dis-*  
803 *cussions* .

804 Banner, M. L., Morison, R. P., 2006. On modeling spectral dissipation due  
805 to wave breaking for ocean wind waves. In: *Proceedings of the 9th Inter-*  
806 *national workshop on wave hindcasting and forecasting*, Victoria, Canada.

807 Banner, M. L., Young, I. R., 1994. Modeling spectral dissipation in the  
808 evolution of wind waves. part I: assessment of existing model performance.  
809 *J. Phys. Oceanogr.* 24 (7), 1550–1570.  
810 URL [http://ams.allenpress.com/archive/1520-0485/24/7/pdf/  
811 i1520-0485-24-7-1550.pdf](http://ams.allenpress.com/archive/1520-0485/24/7/pdf/i1520-0485-24-7-1550.pdf)

812 Barrick, D. E., Headrick, J. M., Bogle, R. W., Crombie, D. D., 1974. Sea  
813 backscatter at HF: interpretation and utilization of the echo. *Proc. IEEE*  
814 62, 673.

815 Bentamy, A., Grodsky, S. A., Carton, J. A., Croizé-Fillon, D., Chapron, B.,  
816 2012. The era-interim reanalysis: configuration and performance of the  
817 data assimilation system. *J. Geophys. Res.* 117, C02011.

818 Bentamy, A., Grodsky, S. A., Chapron, B., Carton, J. A., 2013. Compatibility  
819 of C- and Ku-band scatterometer winds: ERS-2 and QuikSCAT. *J. Mar.*  
820 *Sys.* 117–118, 72–80.

821 Bentamy, A., Piollé, J. F., Prevost, C., 2018. Product user manual for wind  
822 product WIND\_GLO\_WIND\_L4\_REP\_OBSERVATIONS\_012\_006. Tech.  
823 Rep. CMEMS-WIND-PUM-012-006, EU Copernicus Marine Service.

824 Bidlot, J., 2005. Use of Mercator surface currents in the ECMWF forecasting  
825 system. Tech. Rep. Memorandum R60.9/JB/10104, Research Department,  
826 ECMWF, Reading, U. K.

827 Bidlot, J., Janssen, P., Abdalla, S., 2005. A revised formulation for ocean  
 828 wave dissipation in CY25R1. Tech. Rep. Memorandum R60.9/JB/0516,  
 829 Research Department, ECMWF, Reading, U. K.

830 Bidlot, J., Janssen, P., Abdalla, S., 2007. A revised formulation of ocean wave  
 831 dissipation and its model impact. Tech. Rep. Memorandum 509, ECMWF,  
 832 Reading, U. K.

833 Boudière, E., Maisondieu, C., Ardhuin, F., Accensi, M., Pineau-Guillou, L.,  
 834 Lepesqueur, J., 2013. A suitable metocean hindcast database for the design  
 835 of marine energy converters. *Int. J. Mar. Energy* 28 (3–4), e40–e52.

836 Boutin, G., Ardhuin, F., Dumont, D., Sévigny, C., Girard-Ardhuin, F., 2018.  
 837 Floe size effects on wave-ice interactions: theoretical background, imple-  
 838 mentation and applications. *J. Geophys. Res.* 123, 4779–4805.

839 Cavaleri, L., Bertotti, L., 1997. In search of the correct wind and wave fields  
 840 in a minor basin. *Mon. Weather Rev.* 125 (8), 1964–1975.  
 841 URL [http://ams.allenpress.com/archive/1520-0493/125/11/pdf/  
 842 i1520-0493-125-8-1964.pdf](http://ams.allenpress.com/archive/1520-0493/125/11/pdf/i1520-0493-125-8-1964.pdf)

843 Chawla, A., Tolman, H. L., 2008. Obstruction grids for spectral wave models.  
 844 *Ocean Modelling* 22, 12–25.

845 Chawla, A., Tolman, H. L., Gerald, V., Spindler, D., Spindler, T., Alves,  
 846 J.-H. G. M., Cao, D., Hanson, J. L., Devaliere, E.-M., 2013. A multigrid  
 847 wave forecasting model: A new paradigm in operational wave forecasting.  
 848 *Weather and Forecasting* 28, 1057–1078.

849 Chen, G., Belcher, S. E., 2000. Effects of long waves on wind-generated waves.  
 850 *J. Phys. Oceanogr.* 30, 2246–2256.  
 851 URL <http://tinyurl.com/38cbjnk>

852 Chen, G., Chapron, B., Ezraty, R., Vandemark, D., 2002. A global view of  
 853 swell and wind sea climate in the ocean by satellite altimeter and scat-  
 854 terometer. *J. Atmos. Ocean Technol.* 19, 1849–1859.

855 Datawell, 2014. Datawell - high frequency heave resonance. Tech. Rep. see  
 856 <https://www.youtube.com/watch?v=OlrCKTnrhbQ>.  
 857 URL <https://www.youtube.com/watch?v=OlrCKTnrhbQ>



- 858 De Carlo, M., Ardhuin, F., Pichon, A. L., 2020. Atmospheric infrasound  
859 radiation from ocean waves in finite depth: a unified generation theory  
860 and application to radiation patterns. *Geophys. J. Int.* 221, 569–585.
- 861 De Carlo, M., Hupe, P., Le Pichon, A., Ardhuin, F., 2021. Global microbarom  
862 patterns: a first confirmation of the theory for source and propagation.  
863 *Geophys. Res. Lett.* in press.
- 864 Dee, D. P., Uppala, S. M., Simmons, A. J., Berrisford, P., Poli, P., Kobayashi,  
865 S., Andrae, U., Balmaseda, M. A., Balsamo, G., Bauer, P., Bechtold, P.,  
866 Beljaars, A. C. M., van de Berg, L., Bidlot, J., Bormann, N., Delsol, C.,  
867 Dragani, R., Fuentes, M., Geer, A. J., Haimbergere, L., Healy, S. B., Hers-  
868 bach, H., Holm, E. V., Isaksena, L., Køallberg, P., Köhler, M., Matricardi,  
869 M., McNally, A. P., Monge-Sanz, B. M., Morcrette, J.-J., Park, B.-K.,  
870 Peubey, C., de Rosnay, P., Tavolato, C., Thépaut, J.-N., Vitart, F., 2011.  
871 The era-interim reanalysis: configuration and performance of the data as-  
872 simulation system. *Quart. Journ. Roy. Meteorol. Soc.* 137, 553–597.
- 873 Doble, M. J., Bidlot, J.-R., 2013. Wave buoy measurements at the Antarctic  
874 sea ice edge compared with an enhanced ECMWF WAM: Progress towards  
875 global waves-in-ice modelling. *Ocean Modelling* 70, 166–173.
- 876 Doble, M. J., Coon, M. D., Wadhams, P., 2003. Pancake ice formation in the  
877 weddell sea. *J. Geophys. Res.* 108 (C7), 3209.
- 878 Dobler, D., Huck, T., Maes, C., Grima, N., Blanke, B., Martinez, E., Ard-  
879 huin, F., 2019. Large impact of stokes drift on the fate of surface floating  
880 debris in the south indian basin 148, 202–209.
- 881 Dodet, G., Piolle, J.-F., Quilfen, Y., Abdalla, S., Accensi, M., Ardhuin, F.,  
882 Ash, E., Bidlot, J.-R., Gommenginger, C., Marechal, G., Passaro, M.,  
883 Quartly, G., Stopa, J., Timmermans, B., Young, I., Cipollini, P., Donlon,  
884 C., 2020. The sea state cci dataset v1: towards a sea state climate data  
885 record based on satellite observations. *Earth System Sci. Data* 12, 1929–  
886 1951.
- 887 ECMWF, 2019. IFS Documentation CY46R1, Part VII: ECMWF Wave  
888 Model. Tech. Rep. 333, ECMWF, Reading, UK, 103 pp.  
889 URL <https://www.ecmwf.int/node/19311>

890 Elfouhaily, T., Chapron, B., Katsaros, K., Vandemark, D., 1997. A unified  
891 directional spectrum for long and short wind-driven waves. *J. Geophys.*  
892 *Res.* 102 (C7), 15781–15796.

893 Elipot, S., Lumpkin, R., Perez, R. C., Lilly, J. M., Early, J. J., Sykulski,  
894 A. M., 2016. A global surface drifter data set at hourly resolution. *J. Geo-*  
895 *phys. Res.* 121, 2937–2966.

896 ESA, May 2019. Report for mission selection: SKIM. Tech. Rep.  
897 ESA-EOPSM-SKIM-RP-3550, European Space Agency, Noordwijk, The  
898 Netherlands.

899 Farrell, W. E., Munk, W., 2010. Booms and busts in the deep. *J. Phys.*  
900 *Oceanogr.* 40 (9), 2159–2169.

901 Fraser, C. I., Morrison, A. K., Hogg, A. M., Macaya, E. C., van Sebille, E.,  
902 Ryan, P. G., Padovan, A., Jack, C., Valdivia, N., Waters, J. M., 2018.  
903 Antarctica’s ecological isolation will be broken by storm-driven dispersal  
904 and warming. *Nature Climate Change* 8, 704–708.

905 Gelaro, R., McCarty, W., Suárez, M. J., Todling, R., Molod, A., Takacs,  
906 L., Randles, C. A., Darmenov, A., Bosilovich, M. G., Reichle, R., et al.,  
907 2017. The modern-era retrospective analysis for research and applications,  
908 version 2 (merra-2). *Journal of climate* 30 (14), 5419–5454.

909 Girard-Ardhuin, F., Ezraty, R., 2012. Enhanced arctic sea ice drift estimation  
910 merging radiometer and scatterometer data. *IEEE Trans. on Geosci. and*  
911 *Remote Sensing* 50, 2639–2648.

912 Hanafin, J., Quilfen, Y., Ardhuin, F., Sienkiewicz, J., Queffelec, P., Obreb-  
913 ski, M., Chapron, B., Reul, N., Collard, F., Corman, D., de Azevedo,  
914 E. B., Vandemark, D., Stutzmann, E., 2012. Phenomenal sea states and  
915 swell radiation: a comprehensive analysis of the 12-16 February 2011 North  
916 Atlantic storms. *Bull. Amer. Meteorol. Soc.* 93, 1825–1832.

917 Hasselmann, S., Hasselmann, K., 1985. Computation and parameterizations  
918 of the nonlinear energy transfer in a gravity-wave spectrum. part I: a new  
919 method for efficient computations of the exact nonlinear transfer. *J. Phys.*  
920 *Oceanogr.* 15, 1369–1377.

- 921 Hersbach, H., Bell, B., Berrisford, P., Hirahara, S., Horányi, A., Muñoz-  
 922 Sabater, J., Nicolas, J., Peubey, C., Radu, R., Schepers, D., Simmons,  
 923 A., Soci, C., Abdalla, S., Abellan, X., Balsamo, G., Bechtold, P., Biavati,  
 924 G., Bidlot, J., Bonavita, M., Chiara, G. D., Dahlgren, P., Dee, D., Dia-  
 925 mantakis, M., Dragani, R., Flemming, J., Forbes, R., Fuentes, M., Geer,  
 926 A., Haimberger, L., Healy, S., Hogan, R. J., Hólm, E., Janisková, M.,  
 927 Keeley, S., Laloyaux, P., Lopez, P., Lupu, C., Radnoti, G., de Rosnay,  
 928 P., Rozum, I., Vamborg, F., Villaume, S., Thépaut, J., 2020. The ERA5  
 929 global reanalysis. *Quart. Journ. Roy. Meteorol. Soc.* 146, 1999–2049.
- 930 Hersbach, H., Bidlot, J. R., 2008. The relevance of ocean surface current  
 931 in the ECMWF analysis and forecast system. In: *Proceedings from the*  
 932 *ECMWF Workshop on Atmosphere-Ocean Interaction*, 10-12 November  
 933 2008. ASCE.  
 934 URL [www.ecmwf.int/publications/library/do/references/list/](http://www.ecmwf.int/publications/library/do/references/list/28022009)  
 935 [28022009](http://www.ecmwf.int/publications/library/do/references/list/28022009)
- 936 Janssen, P. A. E. M., 1991. Quasi-linear theory of wind wave generation  
 937 applied to wave forecasting. *J. Phys. Oceanogr.* 21, 1631–1642, see com-  
 938 ments by D. Chalikov, *J. Phys. Oceanogr.* 1993, vol. 23 pp. 1597–1600.  
 939 URL [http://journals.ametsoc.org/doi/pdf/10.1175/1520-0485%](http://journals.ametsoc.org/doi/pdf/10.1175/1520-0485%281991%29021%3C1631%3AQLTOWW%3E2.0.CO%3B2)  
 940 [281991%29021%3C1631%3AQLTOWW%3E2.0.CO%3B2](http://journals.ametsoc.org/doi/pdf/10.1175/1520-0485%281991%29021%3C1631%3AQLTOWW%3E2.0.CO%3B2)
- 941 Kuik, A. J., van Vledder, G. P., Holthuijsen, L. H., 1988. A method for the  
 942 routine analysis of pitch-and-roll buoy wave data. *J. Phys. Oceanogr.* 18,  
 943 1020–1034.  
 944 URL [http://journals.ametsoc.org/doi/pdf/10.1175/1520-0485%](http://journals.ametsoc.org/doi/pdf/10.1175/1520-0485%281987%29017%3C0845%3ATROWDT%3E2.0.CO%3B2)  
 945 [281987%29017%3C0845%3ATROWDT%3E2.0.CO%3B2](http://journals.ametsoc.org/doi/pdf/10.1175/1520-0485%281987%29017%3C0845%3ATROWDT%3E2.0.CO%3B2)
- 946 Leckler, F., 2013. Observation et modélisation du déferlement des vagues.  
 947 Ph.D. thesis, Université Européenne de Bretagne, Ecole doctorale des Sci-  
 948 ences de la Mer, Brest, France.  
 949 URL <http://tinyurl.com/leckler-thesis>
- 950 Leckler, F., Ardhuin, F., Filipot, J.-F., Mironov, A., 2013. Dissipation source  
 951 terms and whitecap statistics. *Ocean Modelling* 70 (9), 62–74.
- 952 Lecocq, T., Ardhuin, F., Collin, F., Camelbeeck, T., 2019. On the extraction  
 953 of microseismic groundmotion from analog seismograms for the validation  
 954 of ocean-climate models. *Seismol. Res. Lett.* 91, 1518–1530.

Leonard, B. P., 1991. The ULTIMATE conservative difference scheme applied to unsteady one-dimensional advection. *Computational Methods in Applied Mechanical Engineering* 88, 17–74.

Lumpkin, R., Özgökmen, T., Centurioni, L., 2017. Advances in the application of surface drifters. *Annu. Rev. Mar. Sci.* 9, 6.1–6.23.

Marechal, G., Ardhuin, F., 2020. Surface currents and significant wave height gradients: matching numerical models and high-resolution altimeter wave heights in the agulhas current region. *J. Geophys. Res.* in press.

Mentaschi, L., Besio, G., Cassola, F., Mazzino, A., 2015. Performance evaluation of WAVEWATCH III in the mediterranean sea. *Ocean Modelling* 90, 82–94.

Mulet, S., Rio, M.-H., Etienne, H., Artana, C., Cancet, M., Dibarboure, G., Feng, H., Husson, R., Picot, N., Provost, C., et al., 2021. The new cnes-cls18 global mean dynamic topography. *Ocean Science Discussions* , 1–31.

Munk, W., 2009. An inconvenient sea truth: Spread, steepness, and skewness of surface slopes. *Annu. Rev. Mar. Sci.* 1, 377–415.

Nishida, K., Takagi, R., 2016. Teleseismic S wave microseisms. *Science* 353, 919–921.

Nouguier, F., Mouche, A., Rascle, N., Chapron, B., Vandemark, D., 2016. Analysis of dual-frequency ocean backscatter measurements at Ku- and Ka-bands using near-nadir incidence GPM radar data. *IEEE Geoscience And Remote Sensing Letters* 31, 2023–2245.

Onink, V., Wichmann, D., Delandmeter, P., van Sebille, E., Mar. 2019. The role of Ekman currents, geostrophy and Stokes drift in the accumulation of floating microplastic . *J. Geophys. Res.* 124, 1474–1490.

Perignon, Y., Ardhuin, F., Cathelain, M., Robert, M., 2014. Swell dissipation by induced atmospheric shear stress. *J. Geophys. Res.* 119, 6622–6630.

Peureux, C., Ardhuin, F., 2016. Ocean bottom pressure records from the cascadia array and short surface gravity waves. *J. Geophys. Res.* 121, 2862–2873.

986 Peureux, C., Ardhuin, F., Guimaraes, P. V., 2020. On the unsteady steep-  
 987 ening of short gravity waves near the crests of longer waves in the absence  
 988 of generation or dissipation. *J. Geophys. Res.* .

989 Peureux, C., Benetazzo, A., Ardhuin, F., 2018. Note on the directional prop-  
 990 erties of meter-scale gravity waves. *Ocean Science* 14, 41–52.

991 Phillips, O. M., 1985. Spectral and statistical properties of the equilibrium  
 992 range in wind-generated gravity waves. *J. Fluid Mech.* 156, 505–531.

993 Pineau-Guillou, L., Ardhuin, F., Bouin, M.-N., Redelsperger, J.-L., Chapron,  
 994 B., Bidlot, J., Quilfen, Y., 2018. Strong winds in a coupled wave-  
 995 atmosphere model during a north Atlantic storm event: evaluation against  
 996 observations. *Quart. Journ. Roy. Meteorol. Soc.* 144, 317–332.

997 Quilfen, Y., Chapron, B., 2019. Ocean surface wave-current signatures from  
 998 satellite altimeter measurements. *Geophys. Res. Lett.* 216, 253–261.

999 Quilfen, Y., Chapron, B., Vandemark, D., 2004. The ERS scatterometer  
 1000 wind measurement accuracy: evidence of seasonal and regional biases. *J.*  
 1001 *Atmos. Ocean Technol.* 18, 1684–1697.  
 1002 URL [http://ams.allenpress.com/archive/1520-0426/18/10/pdf/  
 1003 i1520-0426-18-10-1684.pdf](http://ams.allenpress.com/archive/1520-0426/18/10/pdf/i1520-0426-18-10-1684.pdf)

1004 Rapizo, H., Durrant, T. H., Babanin, A. V., 2018. Current-induced dissipa-  
 1005 tion in spectral wave models. *Ocean Dynamics* 68, 939–955.

1006 Rasche, N., Ardhuin, F., 2013. A global wave parameter database for geo-  
 1007 physical applications. part 2: model validation with improved source term  
 1008 parameterization. *Ocean Modelling* 70, 174–188.

1009 Rasche, N., Ardhuin, F., Queffelec, P., Croizé-Fillon, D., 2008. A global  
 1010 wave parameter database for geophysical applications. part 1: wave-  
 1011 current-turbulence interaction parameters for the open ocean based on  
 1012 traditional parameterizations. *Ocean Modelling* 25, 154–171.  
 1013 URL <http://hal.archives-ouvertes.fr/hal-00201380/>

1014 Renault, L., Molemaker, M. J., McWilliams, J. C., Shchepetkin, A. F.,  
 1015 Lemarié, F., Chelton, D., Illig, S., Hall, A., 2016. Modulation of wind work  
 1016 by oceanic current interaction with the atmosphere. *J. Phys. Oceanogr.* 46,  
 1017 1685–1704.

1018 Retailleau, L., Boué, P., Stehly, L., Campillo, M., 2017. Locating microseism  
1019 sources using spurious arrivals in intercontinental noise correlations. *J.*  
1020 *Geophys. Res.* 122, 8107–8120.

1021 Rio, M.-H., Mulet, S., Picot, N., 2014. Beyond GOCE for the ocean circu-  
1022 lation estimate: Synergetic use of altimetry, gravimetry, and in situ data  
1023 provides new insight into geostrophic and Ekman currents. *Geophys. Res.*  
1024 *Lett.* 41, 8918–8925.

1025 Rivas, M. B., Stoffelen, A., 2019. Characterizing ERA-Interim and ERA5  
1026 surface wind biases using ASCAT. *Ocean Sci.* 15, 831–852.

1027 Roarty, H., Cook, T., Hazard, L., George, D., Harlan, J., Cosoli, S., Wyatt,  
1028 L., Fanjul, E. A., Terrill, E., Otero, M., Largier, J., Glenn, S., Ebuchi, N.,  
1029 Whitehouse, B., Bartlett, K., Mader, J., Rubio, A., Corgnati, L., Man-  
1030 tovani, C., Griffa, A., Reyes, E., Lorente, P., Flores-Vidal, X., Saavedra-  
1031 Matta, K. J., Rogowski, P., Prukpitikul, S., Lee, S.-H., Lai, J.-W., Guerin,  
1032 C.-A., Sanchez, J., Hansen, B., Grilli, S., 2019. The global high frequency  
1033 radar network. *Frontiers in Marine Sci.* 6, 164:1–164:23.

1034 Roland, A., Ardhuin, F., 2014. On the developments of spectral wave models:  
1035 numerics and parameterizations for the coastal ocean. *Ocean Dynamics*  
1036 64 (6), 833–846.

1037 Romero, L., 2019. Distribution of surface wave breaking fronts. *Geophys.*  
1038 *Res. Lett.* 46, 10463–10474.

1039 Romero, L., Lenain, L., Melville, W. K., 2017. Observations of surface wave-  
1040 current interaction. *J. Phys. Oceanogr.* 47, 615–632.

1041 Saha, S., Moorthi, S., Pan, H.-L., Wu, X., Wang, J., Nadiga, S., Tripp, P.,  
1042 Kistler, R., Woollen, J., Behringer, D., Liu, H., Stokes, D., Grumbine, R.,  
1043 Gayno, G., Wang, J., Hou, Y.-T., ya Chuang, H., Juang, H.-M. H. a. J. S.,  
1044 Iredell, M., Treadon, R., Kleist, D., Delst, P. V., Keyser, D., Derber, J.,  
1045 Ek, M., Meng, J., Wei, H., Yang, R., Lord, S., van den Dool, H., Kumar,  
1046 A., Wang, W., Long, C., Chelliah, M., Xue, Y., Huang, B., Schemm, J.-K.,  
1047 Ebisuzaki, W., Lin, R., Xie, P., Chen, M., Zhou, S., Higgins, W., Zou, C.-  
1048 Z., Liu, Q., Chen, Y., Han, Y., Cucurull, L., Reynolds, R. W., Rutledge,  
1049 G., Goldberg, M., 2010. The NCEP Climate Forecast System Reanalysis.  
1050 *Bull. Amer. Meterol. Soc.* 91, 1015–1057.



- 1051 Sharmar, V. D., Markina, M. Y., Gulev, S. K., 2021. Global ocean wind-wave  
1052 model hindcasts forced by different reanalyzes: A comparative assessment.  
1053 J. Geophys. Res. 126.
- 1054 Smith, W. H. F., Scharroo, R., 2015. Waveform aliasing in satellite radar  
1055 altimetry. IEEE TGRS 53, 1671–1682.
- 1056 Stopa, J. E., Ardhuin, F., Bababin, A., Zieger, S., 2016a. Comparison and  
1057 validation of physical wave parameterizations in spectral wave models.  
1058 Ocean Modelling 103, 2–17.
- 1059 Stopa, J. E., Ardhuin, F., Girard-Ardhuin, F., 2016b. Wave climate in the  
1060 Arctic 1992-2014: seasonality and trends. The Cryosphere 10, 1605–1629.
- 1061 Stopa, J. E., Ardhuin, F., Stutzmann, E., Lecocq, T., 2019. Sea state trends  
1062 and variability: consistency between models, altimeters, buoys, and seismic  
1063 data (1979-2016). J. Geophys. Res. 124, in press.
- 1064 Stutzmann, E., Schimmel, M., Ardhuin, F., 2012. Modeling long-term seismic  
1065 noise in various environments. Geophys. J. Int. 191, 707–722.
- 1066 The WAVEWATCH III<sup>®</sup> Development Group, 2019. User manual and sys-  
1067 tem documentation of WAVEWATCH III<sup>®</sup> version 6.07. Tech. Note 333,  
1068 NOAA/NWS/NCEP/MMAB, College Park, MD, USA, 465 pp. + Appen-  
1069 dices.
- 1070 Thomson, J., Ackley, S., Girard-Ardhuin, F., Ardhuin, F., Babanin, A.,  
1071 Boutin, G., Brozena, J., Cheng, S., Collins, C., Doble, M., Fairall, C.,  
1072 Guest, P., Gebhardt, C., Gemmrich, J., Graber, H. C., Holt, B., Lehner,  
1073 S., Lund, B., Meylan, M. H., Maksym, T., Montiel, F., Perrie, W., Persson,  
1074 O., Rainville, L., Rogers, W. E., Shen, H., Shen, H., Squire, V., Stammer-  
1075 john, S., Stopa, J., Smith, M. M., Sutherland, P., Wadhams, P., 2018.  
1076 Overview of the arctic sea state and boundary layer physics program. J.  
1077 Geophys. Res. 123.
- 1078 Thomson, J., D’Asaro, E. A., Cronin, M. F., Rogers, W. E., Harcourt, R. R.,  
1079 Shcherbina, A., 2013. Waves and the equilibrium range at ocean weather  
1080 station P. J. Geophys. Res. 118, 595–5962.
- 1081 Tolman, H. L., 1995. On the selection of propagation schemes for a spectral  
1082 wind wave model. Office Note 411, NWS/NCEP, 30 pp + figures.

1083 Tolman, H. L., 2002. Alleviating the garden sprinkler effect in wind wave  
1084 models. *Ocean Modelling* 4, 269–289.

1085 Tolman, H. L., 2008. A mosaic approach to wind wave modeling. *Ocean*  
1086 *Modelling* 25, 35–47.

1087 Tournadre, J., Bouhier, N., Girard-Ardhuin, F., Rémy, F., 2016. Antarctic  
1088 iceberg distributions 2002–2010. *J. Geophys. Res.* 121, 327–349.

1089 Tournadre, J., Poisson, J. C., Steunou, N., Picard, B., 2015. Validation of  
1090 AltiKa matching pursuit rain flag. *Marine Geodesy* 38, 107–1023.

1091 van Vledder, G. P., 2006. The WRT method for the computation of non-linear  
1092 four-wave interactions in discrete spectral wave models. *Coastal Eng.* 53,  
1093 223–242.

1094 WAMDI Group, 1988. The WAM model - a third generation ocean wave  
1095 prediction model. *J. Phys. Oceanogr.* 18, 1775–1810.  
1096 URL [http://journals.ametsoc.org/doi/pdf/10.1175/1520-0485%](http://journals.ametsoc.org/doi/pdf/10.1175/1520-0485%281988%29018%3C1775%3ATWMTG0%3E2.0.CO%3B2)  
1097 [281988%29018%3C1775%3ATWMTG0%3E2.0.CO%3B2](http://journals.ametsoc.org/doi/pdf/10.1175/1520-0485%281988%29018%3C1775%3ATWMTG0%3E2.0.CO%3B2)

1098 Williams, G., Maksym, T., Wilkinson, J., Kunz, C., Murphy, C., Kimball,  
1099 P., Singh, H., 2014. Thick and deformed antarctic sea ice mapped with  
1100 autonomous underwater vehicles. *Nature Geosci.* 8, 61–67.

1101 Wunsch, C., Ferrari, R., 2009. Ocean circulation kinetic energy:reservoirs,  
1102 sources, and sinks. *Annu. Rev. Fluid Mech.* 41, 253–282.

1103 Yueh, S. H., Wilson, W. J., Dinardo, S. J., Hsiao, S. V., 2006. Polarimet-  
1104 ric microwave wind radiometer model function and retrieval testing for  
1105 windsat. *IEEE Trans. on Geosci. and Remote Sensing* 44 (3), 584–595.